1st CWE Workshop 2022

Advanced modeling of stochastic Wind Effects and Vibrations

Book of Abstracts

26th October 2022

Center for Wind and Earthquake Engineering
RWTH Aachen University

Workshop Program

Outline

The impact of climatic actions on building structures has raised more and more interest in the past decades for different reasons. On the one hand, there is an ongoing tendency for challenging architectural designs and higher-strength materials, leading to more lightweight and load-sensitive structures. On the other hand, the world climate is changing with unclear impact on specific wind effects in terms of intensity and frequency of occurrence. Due to lively ongoing research, advanced analytical, numerical, and data-based methods, the field of wind engineering provides the necessary means for adjusted and realistic load recommendations, higher material-efficiency and safer structural designs. The workshop aims to gather current research and to initiate further collaboration.

Scope and Focus

With a particular focus on wind-induced actions, the Center of Wind and Earthquake Engineering of RWTH Aachen University invites international scholars to a "Workshop on Advanced modeling of stochastic Wind Effects and Vibrations". The CWE wants to organize this workshop event to allow insights into ongoing international research, deepen the scientific network, reflect on the possible impact of climate change on the wind engineering discipline, and discuss new concepts for modeling wind-induced effects.

Keynote Lecture

The keynote lecture to the CWE workshop was provided by Prof. Ahsan Kareem, who is one of the world outstanding experts in the field of wind engineering and data analysis in the context of natural hazards. Further information of his impressive career can be found under: NotreDame-USA at the university of NotreDame, USA.

The topic of the keynote was:
"Emerging frontiers in wind engineering: Computing, stochastics, machine learning and beyond".

Contributions

The workshop was organized in three thematic sections:

- Section 1: Wind Climate and its numerical Representation
- Section 2: Vortex induced Vibrations and Aeroelasticity
- Section 3: Gust Response and Realdata Analysis

All participants have handed in abstracts, which the organizers appreciated very much. The detailed contributions are listed in an overview on the following page.

CWE thanks all presenting participants for supporting the workshop with presentations, abstracts and all particpants (including the webinar) for the active discussion!

Prof. Dr.-Ing. Markus Feldmann
Member of the Executive Board, CWE at RWTH Aachen University

Workshop Contributions

Multi-scale numerical simulation of typhoon wind effects on urban environments

Sunce Liao, Mingfeng Huang[1*]

[1]College of Civil and Architecture Engineering, Zhejiang University, Hangzhou 310058, P.R.China.

[*]**Corresponding author**: mfhuang@zju.edu.cn

Abstract

Based on the mesoscale WRF (Weather Research Forecast) model and CFD (Computational Fluid Dynamics) simulation, a coupling numerical simulation framework aiming to resolve typhoon wind field around urban blocks has been developed in this paper. This framework mainly consists of the mesoscale model, microscale CFD model and the coupling scheme. Typhoon weather reanalysis and wind field simulation are conducted by the WRF model with nested computational domains incorporating high-resolution topography data. The specific wind profiles generated by the WRF model are applied in the coupling interface as the inlet boundary conditions for the downscaled CFD model with urban building blocks through the interpolation technique. The wind field around the K11 building in Hong Kong during Typhoon Kammuri was simulated by the multi-scale framework, and the simulation result was compared to the full-scale measurement wind speed data at the top of K11 building.

Keywords

typhoon; numerical simulation; WRF; CFD; multi-scale; urban building blocks

1. Introduction

Urbanization is one of the trends of global social development. Rapid urbanization greatly changes the local topography and local wind climate. Highly densified urban regions are especially vulnerable to the impact of natural hazards. Another tendency is climate change. It will increase the number of significant natural hazards, such as typhoons, flooding and drought [1,2]. Otherwise, typhoons bring high winds and heavy rain to coastal cities, along with unique urban aerodynamic behaviors like building disturbance, heat island effects, and complex local topographic conditions, resulting in severe typhoon catastrophe damage and various secondary hazards in urban building masses. A scientific and reasonable description of wind field under typhoon conditions is of great significance to wind load determination of wind-sensitive structures.

The urban wind field under typhoon conditions has generated increasing research interest in recent years. Much work has been reported recently in these field, most of which focus on the field measurement, wind tunnel test as well as numerical simulation. As for the observation of urban wind field under typhoon, He et al., Luo et al. and He et al. carried out a series of field measurement study on the basis of the wind records from 356-m-high Shenzhen Meteorological Gradient Tower[3-5]. Boundary-layer wind tunnels are also a principal tool of wind engineers in urban planning and design projects. Compared with field measurement and wind tunnel tests, numerical simulation is likely to be one of the most promising methods for urban aerodynamics, since it is the most affordable, accurate, and informative[6]. In fact, wind characteristics in the typhoon boundary layer were different from those in the monsoon climate mode. Evident temporal-spatial variability and a multiscale eddy structure could be produced under typhoon conditions[7]. In addition, CFD model is limited by the number of grids so that it cannot adopt too large computational domain. It is difficult to accurately obtain the inlet boundary conditions under typhoon only by CFD model. The mesoscale weather research and forecasting (WRF) mode based on fluid dynamics and thermodynamics can simulate wind velocity field and wind temperature field of a typhoon effectively, with comprehensive considerations to the

evolution, violent changes and attenuation characteristics of a typhoon[8]. Based on the advantages of this two models, Zajaczkowski et al.[9] preliminarily explored the downscaling method. Moreover, a few scholars[10,11] have applied this method to typhoon wind field simulation in recent years.

However, the application of the coupling framework in urban wind field simulation under typhoon conditions is still limited and lack of detailed validation and analysis, especially focusing on the wind field distribution in urban area, turbulence in urban wind field and wind pressure characteristic. Based on WRF model and CFD method, a high fidelity coupling numerical simulation framework of urban wind field during typhoon is implemented in this paper.

2. Numerical methodology

2.1 Weather Research and Forecasting model

The weather Research and Forecasting (WRF) model which has been widely used in mesoscale atmospheric forecasting and scientific research is a new generation of mesoscale meteorological numerical prediction system jointly developed by many scientific research institutions. WRF model can be used to simulate local weather as well as extreme weather occurrences thanks to several physics and dynamics parameterization schemes and data assimilation.

In WRF model, mass-based terrain following coordinate is adopted in the vertical direction[12]. The expression of terrain following coordinate in the vertical direction can be defined as follow:

$$\eta = \frac{p_h - p_{ht}}{p_{hs} - p_{ht}} \tag{1}$$

where p_h is the pressure of a destination location, p_{ht} denotes the pressure along the top boundaries as well as p_{hs} refers to the pressure of the surface layer.

Model discretization is crucial to numerically solve governing equations. For the temporal discretization, the third-order Runge-Kutta time integration scheme is applied in low-frequency mode, while acoustic integration scheme is combined to maintain numerical stability in high-frequency situation. ARW solver adopts variable staggered Arakawa C grid scheme in horizontal domain, which plays a key role in defining the spatial discretization. Furthermore, the ARW solver incorporates multiple physics and dynamics parameterization schemes that can be combined in different ways.

2.2 Computational Fluid Dynamics

Computational Fluid Dynamics (CFD) is an effective technique widely utilized in the automobile, aircraft, and other industries to solve the equations of fluid motion numerically using computers. There are two approaches for numerically solving the resulting governing equations. The first approach is to average these equations in time and then to solve the resulting equations for each cell, i.e., Reynolds averaged Navier-Stokes (RANS). The other approach is to solve the governing equations directly to resolve all turbulent scales in the flow, i.e., Direct Numerical Simulation (DNS). For DNS, the computational cells have to be very small such that practical calculations of DNS are prohibitively high. This leads to large eddy simulation (LES), in which only large turbulence scales are solved

RANS have the advantage of fast calculating speed but poor accuracy while LES method is high precision but consumes a lot of computing resources. Much work has been reported recently in studying RANS/LES hybrid method. Spalart and Allmaras[13] firstly proposed the detached eddy simulation (DES) approach. The core concept of DES is that RANS is used to solve the solution near the wall, while LES is applied away from the wall where the turbulence is fully developed. Moreover, Shur et al.[14] proposed improved delayed detached eddy simulation model (IDDES) which has been used as the turbulence model in this paper. The governing equations of DES method can be transformed to the non-dimensional form as:

$$\frac{\partial \overline{u_i}}{\partial x_i} = 0 \tag{2}$$

$$\frac{\partial \overline{u_i}}{\partial t} + \frac{\partial (\overline{u_i u_j})}{\partial t} = -\frac{1}{\rho}\frac{\partial \bar{p}}{\partial x_i} - \frac{\partial}{\partial x_i}\left(\nu \frac{\partial \overline{u_i}}{\partial x_j}\right) - \frac{\partial \tau_{ij}}{\partial x_j} \tag{3}$$

where u_i and u_j are the velocity component of each direction, p is the pressure as well as ρ and ν represent the density and viscosity, respectively. τ_{ij} is the momentum transport of turbulence which can be defined as:

$$\tau_{ij} = -2\upsilon_T \overline{S_{ij}} \tag{4}$$

$$\overline{S_{ij}} = \frac{1}{2}\left(\frac{\partial \overline{u_i}}{\partial x_j} + \frac{\partial \overline{u_j}}{\partial x_i}\right) \tag{5}$$

where ν_T is the turbulent eddy viscosity and S_{ij} is filtered strain rate tensor.

2.3 Coupling WRF model and CFD model

As shown in Fig. 1, the proposed numerical urban wind field simulation framework can be divided into three components: mesoscale simulation, microscale simulation and coupling interface. The mesoscale simulation task consists of two procedures aiming to resolve typhoon weather process and generate wind profiles as inputs for the downscale simulation. While moving nest grids is employed to simulate the evolution of typhoon, typhoon wind field in a target area is reproduced by fixed grids in next microscale simulation.

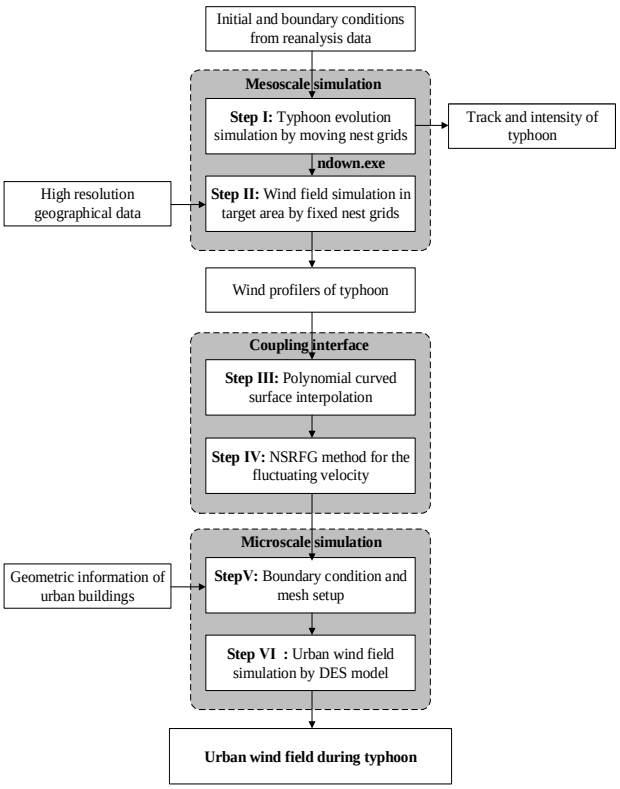

Figure 1. Framework of proposed multi-scale wind field simulation method

The DES model is employed in microscale simulation to capture fluctuating flow field information around building blocks with refined meshes. The lateral boundary conditions of DES run could be determined by the WRF mesoscale simulation. The wind profiles generated by the WRF model are interpolated in the coupling interface as the inlet boundary conditions of the DES model by the polynomial surface interpolation. The narrowband synthesis random flow generator (NSRFG) has been adopt subsequently to generate the appropriate turbulent inflow data as velocity inlet conditions [15].

3. Simulation framework validation

In order to verify the effectiveness of the simulation frame work, typhoon urban wind filed simulation has been carried out for Typhoon Kammuri attacking Hong Kong in 2008. Typhoon Kammuri formed over South China Sea on August 4, 2008(UTC) which intensified into a strong tropical cyclone in the early morning of August 5 and approached Hong Kong at 2:00 on August 6. The simulation is centered on K11 Building in Hong Kong, which has 73 floors and a total height of 270 meters (Fig. 2). An anemometer was deployed on the top floor of K11 Building for continuously recording the wind velocity[16]. The velocity measurement data during Typhoon Kammuri has been used for validation.

Figure 2. Location of k11 Building

3.1 WRF domain and parameters setting

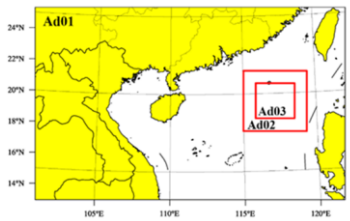

(a) the movable domains

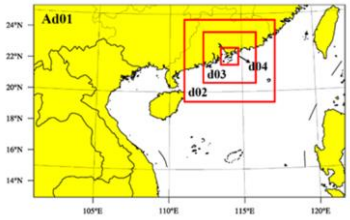

(b) the nested domain

Figure 3. Computational domains of WRF simulation

According to the multi-scale simulation framework, a WRF mesoscale simulation of Typhoon Kammuri was performed firstly. The 72-hour simulation duration is from 0:00 on August 5 to 0:00 on August 8, 2008 (UTC). Fig. 3(a) shows a triply nested grid configuration scheme for typhoon evolution

simulation which contains one fixed domain and two moved domain. In the vertical direction, 36 levels of non-equidistant grids are used in three domains for the WRF simulation. The fixed nested grids are also designed to simulate the wind field in the target area as shown in Fig. 3(b).

Numerical experiments were performed for various microphysics schemes. Fig. 4 depicts the simulated path and intensity results with various microphysics schemes, and compared to the China Meteorological Administration (CMA) observation. It was found that New Thompson scheme seems the best microphysics scheme as the corresponding WRF simulation results agree well with the CMA observation of typhoon path and intensity evolutions.

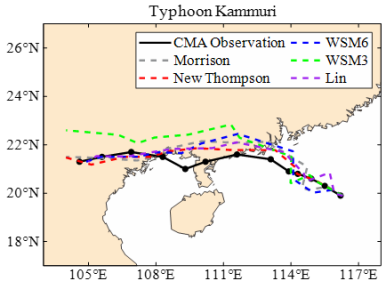

(a) the typhoon track

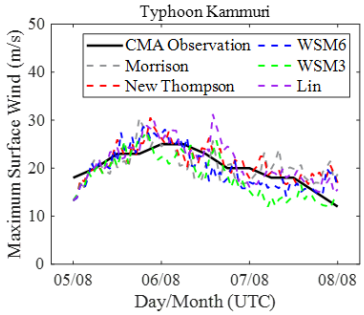

(b) maximum surface wind

Figure 4. Results from the WRF simulation

3.2 DES domain and parameters setting

The size of computational domain is 2000m (length)×2000m (width)×1000m (height). The northern, southern and eastern patches of domain are set as the velocity-inlet boundary whose initial values are provided by the WRF results. All building faces and the ground are defined as no-slip walls, where the wind velocity is set to zero.

Fig. 5 presents the mesh scheme around urban building blocks. The size of background grids is 10m in horizontal direction and gradually increasing from

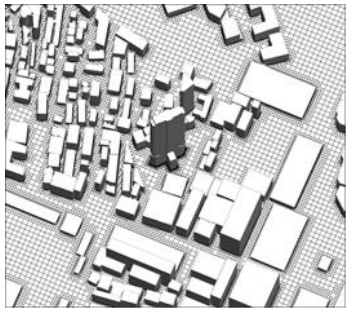

Figure 5. Mesh refinement around building blocks

1m to 50m along vertical direction The minimum grid size is 0.4m and total number of grid cells is 10 million. The trial calculation shows that the simulation requirements are met when the time step is set to 0.2s.

3.3 Evaluation of simulation results

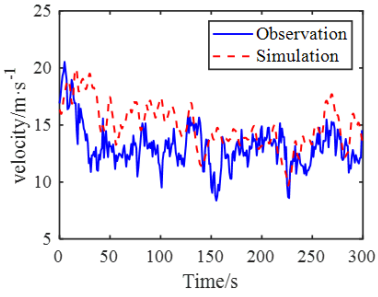

(a) wind velocity

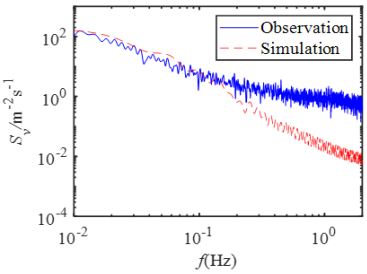

(b) power spectrums

Figure 6. Comparison from simulation and measurement

The 5-mins simulated wind speed (02：30 to 02：35 on August 8, 2008) at the top of K11 building was extracted and compared with the measured results of anemometer, as shown in Fig. 6. It can be seen that the downscaling simulation results are slightly larger than the measured results. Fig. 6(b) gives the simulated power spectrum of fluctuating wind velocity compared with the measured results. It indicates that the low frequency part of the simulation results is in good agreement with the measured spectrum but in the high frequency part of simulated spectrum drops rapidly than the measured. In general, this simulation

framework can well reproduce the wind field around K11 building during Typhoon Kammuri.

4. Conclusions

A coupling numerical simulation framework of typhoon wind fields has been presented in this study which combines the advantages of WRF and CFD. The wind field simulation around K11 Building in Hong Kong during Typhoon Kammuri has been carried out to verify the robustness and accuracy of this framework. The coupling numerical simulation framework is capable of accurately and efficiently simulating the track and the strengthening process of typhoon Kammuri. Urban wind fields under typhoon conditions could be well simulated through this framework.

References

[1] X. Sun et al. “Assessment of climate change impacts and urban flood management schemes in central Shanghai”. In: *International Journal of Disaster Risk Reduction* 65 (2021), pp. 102563. ISSN: 2212-4209.

[2] J. Kossin et al. “Global increase in major tropical cyclone exceedance probability over the past four decades”. In: *Earth, Atmospheric, And Planetary Sciences* 117. 22 (2020), pp. 11975-11980. ISSN: 2212-4209.

[3] Y. Luo et al. “Observation of Typhoon Hato based on the 356-m high meteorological gradient tower at Shenzhen”. In: *Journal of wind engineering and industrial aerodynamics* 207 (2020), pp. 104408. ISSN: 0167-6105.

[4] J. He et al. “Observations of wind and turbulence structures of Super Typhoons Hato and Mangkhut over land from a 356 m high meteorological tower”. In: *Atmospheric Research* 265:105910 (2022). ISSN: 0169-8095.

[5] Q. Li et al. “Impact of a Fifty-Year-Recurrence Super Typhoon on Skyscrapers in Hong Kong: Large-Scale Field Monitoring Study”. In: *Journal of Structural Engineering* 147. 3 (2021), pp. 04021004. ISSN: 0733-9445.

[6] Q. Chen. “Using computational tools to factor wind into architectural environment design”. In: *Energy and Buildings* 36. 12 (2004), pp. 1197-1209. ISSN: 0378-7788.

[7] L. Song et al. “Wind characteristics of a strong typhoon in marine surfaceboundary layer”. In: *Wind and Structures* 15.1 (2012), pp. 1-15. ISSN: 1226-6116.

[8] M. Huang et al. “Multi-scale simulation of time-varying wind fields for Hangzhou Jiubao Bridge during Typhoon Chan-hom”. In: *Journal of Wind Engineering and Industrial Aerodynamics* 179 (2018), pp. 419-437. ISSN: 0167-6105.

[9] F. Zajaczkowski et al. “A preliminary study of assimilating numerical weather prediction data into computational fluid dynamics models for wind prediction”. In: *Journal of Wind Engineering and Industrial Aerodynamics* 99. 4 (2011), pp. 320-329. ISSN: 0167-6105.

[10] T. Takemi et al. “Quantitative Estimation of Strong Winds in an Urban District during Typhoon Jebi (2018) by Merging Mesoscale Meteorological and Large-Eddy Simulations”. In: *SOLA* 15 (2019), pp. 22-27. ISSN: 1349-6476.

[11] S. Ke and R. Zhu. “Typhoon-Induced Wind Pressure Characteristics on Large Terminal Roof Based on Mesoscale and Microscale Coupling”. In: *Journal of Aerospace Engineering* 32.6 (2019), pp. 04019093. ISSN: 0893-1321.

[12] R. Laprise. “The Euler Equations of Motion with Hydrostatic Pressure as an Independent Variable”. In: *Monthly Weather Review* 120. 1 (1992), pp. 197-207. ISSN: 1520-0493

[13] P. Spalart, S. Allmaras 1992. “A one-equation turbulence model for aerodynamic flows.: American Institute of Aeronautics and Astronautics”.

[14] M. Shur et al. “A hybrid RANS-LES approach with delayed-DES and wall-modelled LES capabilities”. In: *International Journal of Heat and Fluid Flow* 29.6(2008), pp. 1638-1649. ISSN: 0142-727X.

[15] Y. Yu et al. “A new inflow turbulence generator for large eddy simulation evaluation of wind effects on a standard high-rise building”. In: *Building and Environment* 138 (2018), pp. 300-313. ISSN: 0360-1323.

[16] M. Huang et al. “Probabilistic assessment of vibration exceedance for a full-scale tall building under typhoon conditions”. In: *The Structural Design of Tall and Special Buildings* 27.15 (2018), pp. e1516. ISSN: 1541-7794.

CFD simulations of extreme thunderstorm downburst winds

Josip Žužul[1]*, Alessio Ricci[2,3], Massimiliano Burlando[1]

[1] *Department of Civil, Chemical and Environmental Engineering, University of Genoa, Genoa, Italy*
[2] *Department of Civil Engineering, KU Leuven, Leuven, Belgium*
[3] *Department of the Built Environment, Eindhoven University of Technology, Eindhoven, the Netherlands*
***Corresponding author**: josip.zuzul@edu.unige.it

Abstract
Thunderstorms are non-synoptic wind events with potentially devastating implications for the integrity of low and mid-rise structures. Thunderstorm outflows commonly referred to as downbursts are characterized by a vertical cold air impingement from the cloud to the surface of the Earth accompanied with a divergent radial outflow dominated by the primary ring vortex. This study aims to investigate the physical characteristics of downbursts in the perspective of wind-induced structural loading. Two downburst scenarios were considered: (*Case 1*) an isolated downburst wind, and (*Case 2*) a downburst immersed in an approaching atmospheric boundary layer (ABL) wind. For that purpose, the experimental tests that were previously performed in WindEEE Dome were recreated through Computational Fluid Dynamics (CFD) simulations. Both *Case 1* and *Case 2* were successfully validated with experiments in terms of vertical profiles of radial velocity. All three utilized CFD approaches (URANS, SAS and LES) showed decent performance. However, the LES demonstrated its superiority over the former two in terms of obtaining physically most meaningful representation of complex downburst flow conditions.

Keywords
Thunderstorm downbursts, CFD simulations, WindEEE Dome, ABL-downburst wind interaction

1. Introduction

Severe non-synoptic winds with thunderstorm-related origin (downbursts and tornados) are known for their potential to create significant damage to low-rise structures [1]. In that regard, the most recent ASCE 7-22 standards have been updated to account for tornados, while the Eurocode is about to follow the same example [7]. A similar approach for downbursts is however still not present [9], implying that further research on downbursts is necessary. In the most simplified case, the physical characteristics of a downburst are defined through the vertical cold air impingement from the storm that produces the primary ring vortex which leads to the strong diverging winds close to the surface [3]. However, a realistic downburst would rather incorporate the additional contribution of the atmospheric boundary layer (ABL) winds in which it is commonly immersed. This contribution of ABL winds causes the downburst flow field to deflect from the theoretically symmetric one found in the isolated storms. This therefore yields a requirement for a comparative study of flow field behavior between these two scenarios in the perspective of identifying the worst conditions in terms of wind loading of structures. In this work two downburst scenarios were selected for the investigation of flow characteristics: (*i*) an isolated downburst wind, and (*ii*) a downburst immersed in an approaching ABL wind. This study was conducted within the framework of the Project "THUNDERR – Detection, simulation, modelling and loading of thunderstorm outflows to design wind-safer and cost-efficient structures" [8, 10] and its focus was on the reconstruction of the experimental tests by means of Computational Fluid Dynamics (CFD) technique. In that perspective, the experimental tests previously performed in the WindEEE Dome - a specialized facility for reconstructing downbursts at reduced scales [2], were used as the baseline for CFD analyses. Several CFD approaches were utilized in this study: (*i*) unsteady Reynolds-Averaged Navier-Stokes (URANS), (*ii*) Scale-Adaptive Simulations (SAS), and (*iii*) Large-Eddy Simulations (LES). The selected CFD approaches were also used for the

formulation of best-practice guidelines in the application of the CFD technique for downburst winds. The paper is organized as follows: Section 2 provides the overview of baseline experimental downburst scenarios (isolated downburst, and downburst immersed in an approaching ABL) that were used in the numerical studies. Section 3 summarizes the numerical settings used to conduct the CFD analyses. Section 4 presents the comparison of CFD results with experiments. Finally, Section 5 summarizes the results and presents future work perspectives.

2. Experimental tests

The experimental tests of both isolated thunderstorm downburst and a downburst immersed in an ABL wind were carried out at the WindEEE Dome [2]. The WindEEE Dome is a closed-circuit facility of a hexagonal shape that recreates the near-surface downburst flow through the jet impingement from the nozzle. Conversely, for the generation on ABL-like winds it utilizes 60 fans placed at one sidewall of the chamber (Figure 1). For the isolated downburst tests (*Case 1*), the vertical inflow jet velocity w_{jet} of 9 m/s was released through the inflow jet nozzle of 3.2 m diameter (D). Following the jet release, the primary vortex (PV) forms and the near-surface flow features representative of the full-scale downbursts are recreated. The jet release duration in the chamber was 4 seconds, while the total duration of the experiment was 10 seconds. The experimental campaign made use of a set of Cobra probes placed on a measurement rake to record the radial velocity during the event. The measurement rake was placed at various radial R/D locations (distanced from the chamber center). Experiments were repeated 20 times to obtain a greater degree of statistical significance. In order to recreate the interaction between two wind types (*Case 2*), the experimental tests were performed in two phases. Firstly, the ABL-like wind was developed in the chamber for 24 seconds (two flow-through times), by means of frictional effects induced by the (almost) completely smooth chamber surface. Next, the downburst was released through the vertical jet impingement from the nozzle (w_{jet} of 12 m/s) in the same way as for (*Case 1*). The experimental campaign utilized two sets of Cobra probes to record the velocity time histories: (*i*) Cobras pointing in the direction of the ABL-like wind, and (*ii*) Cobras pointing towards the chamber center to record the downburst-related radial velocities. Cobra probes were mounted on a measurement rake placed across various azimuthal locations α (with respect to the approaching ABL) and radial R/D locations (distanced from the chamber center). The experiments were repeated 10 times to obtain a better statistical representation of the phenomenon. (*Case 1*) considered only the azimuthal position α of 0° due to the assumed flow axisymmetry.

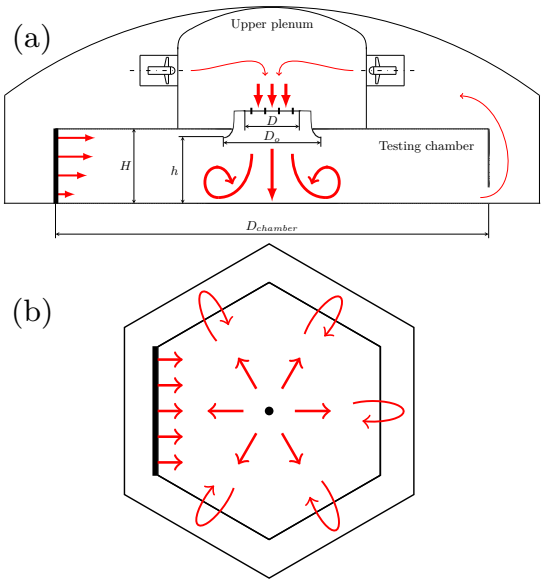

Figure 1. WindEEE Dome facility schematic: (a) front view and, (b) top view of the testing chamber.

3. CFD simulations

3.1 Isolated downburst wind

CFD simulations for the isolated downburst were performed at a computational grid (16.5 million hexahedral cells) representing half of the WindEEE Dome chamber, by taking advantage of the symmetry constraint in order to save computational resources. Wall boundaries were treated with the no-slip condition, while zero-static gauge pressure was specified at the outlet. The near-wall flow was modeled using the Spalding wall functions for smooth surfaces. The PISO-algorithm based solver was adopted to couple pressure and velocity fields, with the usage of second-order discretization schemes. Three CFD approaches were used: URANS, SAS, and LES. The URANS (and SAS) utilized the $k-\omega$ SST turbulence model, while the LES employed the dynamic sub-grid scale turbulence model for the evaluation of Smagorinsky constant through Lagrangian averaging process [5]. The inflow turbulence for LES simulation case was synthesized by adopting the anisotropic turbulent spot method by Kröger and Kornev [4]. Simulations were performed in two stages: (*i*) with the fixed mean vertical inflow velocity of 9 m/s at the nozzle, and (*ii*) with the zero-inflow velocity (*i.e.* by keeping the inflow through the nozzle closed) that would account for the

gradual event dissipation.

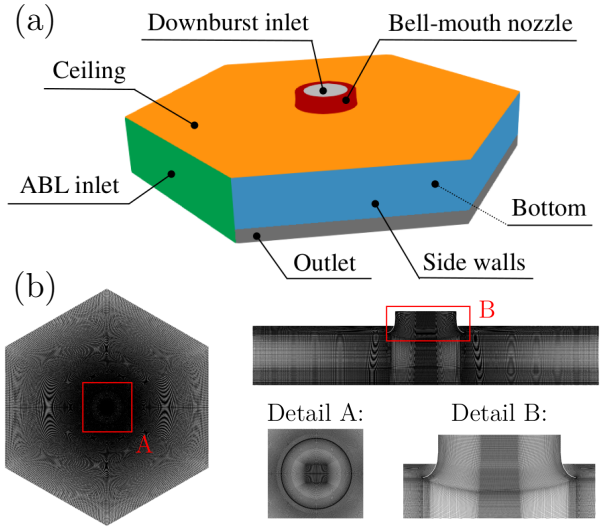

Figure 2. Computational domain with the intication of boundaries for the *Case 2* (a), and corresponding computational grid (b).

3.2 Downburst immersed in an ABL wind

To accurately perform complex downburst-ABL wind interaction, the appropriate approach ABL profile was characterized at the inlet of the computational domain representing the WindEEE Dome testing chamber. The constructed structured grid was composed of 33 million elements described the entire WindEEE Dome testing chamber (Figure 2). The analogous domain and grid configuration (just half of it) was used for the *Case 1*. CFD simulations (URANS, SAS, and LES) were performed in accordance with the experimental campaign: (*i*) ABL-like flow was developed and initialized in the domain, and (*ii*) downburst jet was released from the nozzle inlet with the average vertical jet velocity (w_{jet}) of 12 m/s on the top of the background ABL-like wind. Similarly to the isolated downburst *Case 1*, the $k-\omega$ SST turbulence model was used for the URANS and SAS, while the dynamic model with Lagrangian averaging was used to account for the subgrid scale turbulence in LES simulations. Spatially and temporally correlated turbulent structures needed for the LES simulations at both ABL and downburst inflow faces was introduced through the turbulent inflow generator proposed by Poletto et al. [6]. Wall functions for the atmospheric flows were used at the bottom surface, while the Spalding wall functions were utilized at other wall-type boundaries. Other settings are similar to the ones already introduced for the isolated downburst case: zero-static gauge pressure at the outlet, the second-order discretization schemes were used for the equations and the PISO algorithm-based solver was used to couple pressure and velocity fields.

4. Results

4.1 Isolated downburst wind

CFD results and measured data are compared in terms of vertical profiles of radial velocity component (u) at the selected radial position, *i.e.* in the vicinity of the maximum radial velocity occurrence ($R/D = 1.2$). The comparison is presented in Figure 3 for the selected non-dimensional time steps τ, defined as $\tau = w_{\text{jet}} \cdot t/D$. The velocity u was hereby normalized with the maximum radial velocity registered in LES simulations U_{max}, while the height z was normalized with the height Z_{max} corresponding to the Umax. The measured data is indicated with black dots (ensemble mean across all repetitions) with two-sided error bars of the experimental variability (*i.e.* maximum and minimum occurrence across all repetitions). The CFD simulations generally show acceptable degree of accuracy by falling within the error bars of experimental repetitions throughout the majority of selected time steps. However, URANS and SAS tend to overestimate (τ = 4.725, τ = 6.975) and underestimate (τ = 5.2875, τ = 5.85) the velocity profile during the primary vortex passage, when compared to both experiments and LES. Although all three used CFD approaches provided decent accuracy, the LES simulations show superior behavior by consistently representing the physical behavior of the experimental downburst.

4.2 Downburst immersed in an ABL wind

Figure 4 shows the comparison of measured data with simulated vertical profiles (URANS, SAS, and LES cases) of radial velocity (u) at the rear side ($\alpha = 180°$) at $R/D = 1.4$, and for the selected set of non-dimensional time steps τ. This particular location was selected since the U_{max} was registered in its vicinity (in LES simulations). Additionally, the vertical profiles associated with the isolated jet were also presented to allow for the comparison in terms of profile change due to the presence of the ABL-like winds. In general, the measured and simulated profiles show a very good agreement across all positions of Cobra probes, and across all selected time instances τ. The vertical profiles at $\alpha = 180°$ are found to have a less pronounced nose due to higher values observed at upper levels with respect to profiles at $\alpha = 0°$ (not presented here), which are caused by the higher level ABL winds. Although URANS and SAS approaches gave promising results for the general flow understanding, they are found to have a tendency for the overestimation of the velocity peak associated with the PV passage (not presented

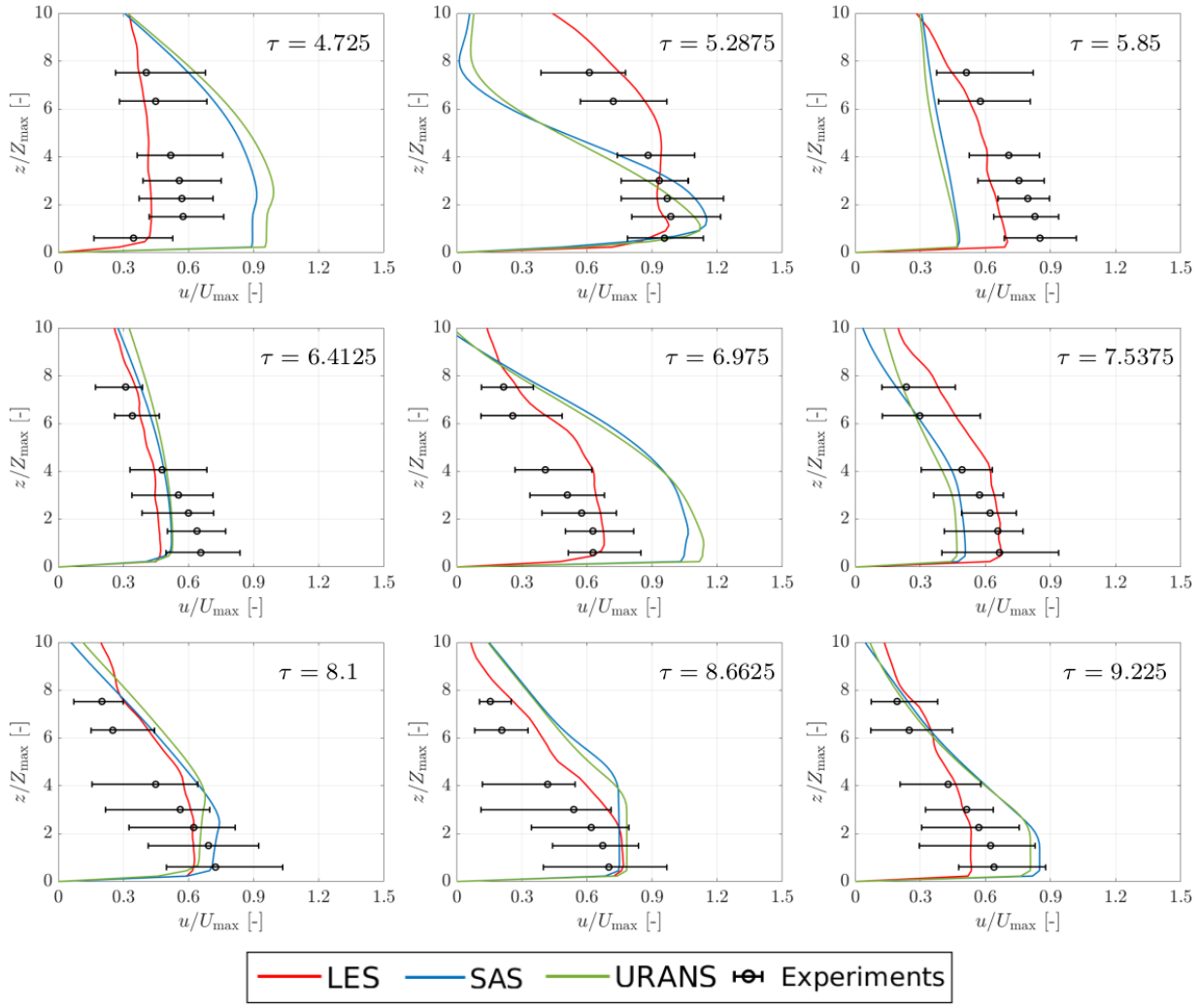

Figure 3. Comparison of measured data with simulated vertical profiles of radial velocity at radial location R/D = 1.2 for a set of non-dimensional time steps (τ).

here). Conversely, LES simulations showed consistent superior performance when compared to the URANS and SAS, and are therefore considered a favorable CFD approach for numerical description of downburst flows in conjuction with the ABL-like winds.

5. Conclusions and future work perspectives

The study presented in this work was conducted under the umbrella of the Project "THUNDERR – Detection, simulation, modelling and loading of thunderstorm outflows to design wind-safer and cost-efficient structures" [8, 10] and it focused on the numerical reconstruction of reduced scale experimental tests previously performed in the WindEEE Dome. In particular, two reduced-scale experimental downburst scenarios were recreated through the application of the CFD technique: (*i*) an isolated downburst wind (*Case 1*), and (*ii*) a downburst immersed in an approach ABL wind (*Case 2*). Both campaigns were recreated through URANS, SAS, and LES approaches, and the numerical results were compared with the measurements in the form of vertical profiles of radial velocity at radial locations (R/D) in the proximity of the location where strongest winds were observed. The comparison with the measurements demonstrated that all three utilized CFD approaches can provide a reasonable degree of accuracy for both analyzed scenarios in terms of a trend of vertical profiles in time. However, the URANS and SAS were found to lack consistency in adequately describing the primary vortex passage. That defficiency in turn resulted in the overestimation and underestimation of the associated radial velocity. Conversely, LES showed a consistent trend and accuracy in predicting the strongest winds in complex flow conditions. Compared to the *Case 1* which showed the axisymmetric flow behavior, the scenario of a downburst immersed in an ABL wind has an emphasized flow asymmetry. All three employed CFD approaches on average provided similar acceptable behavior as in the case of an iso-

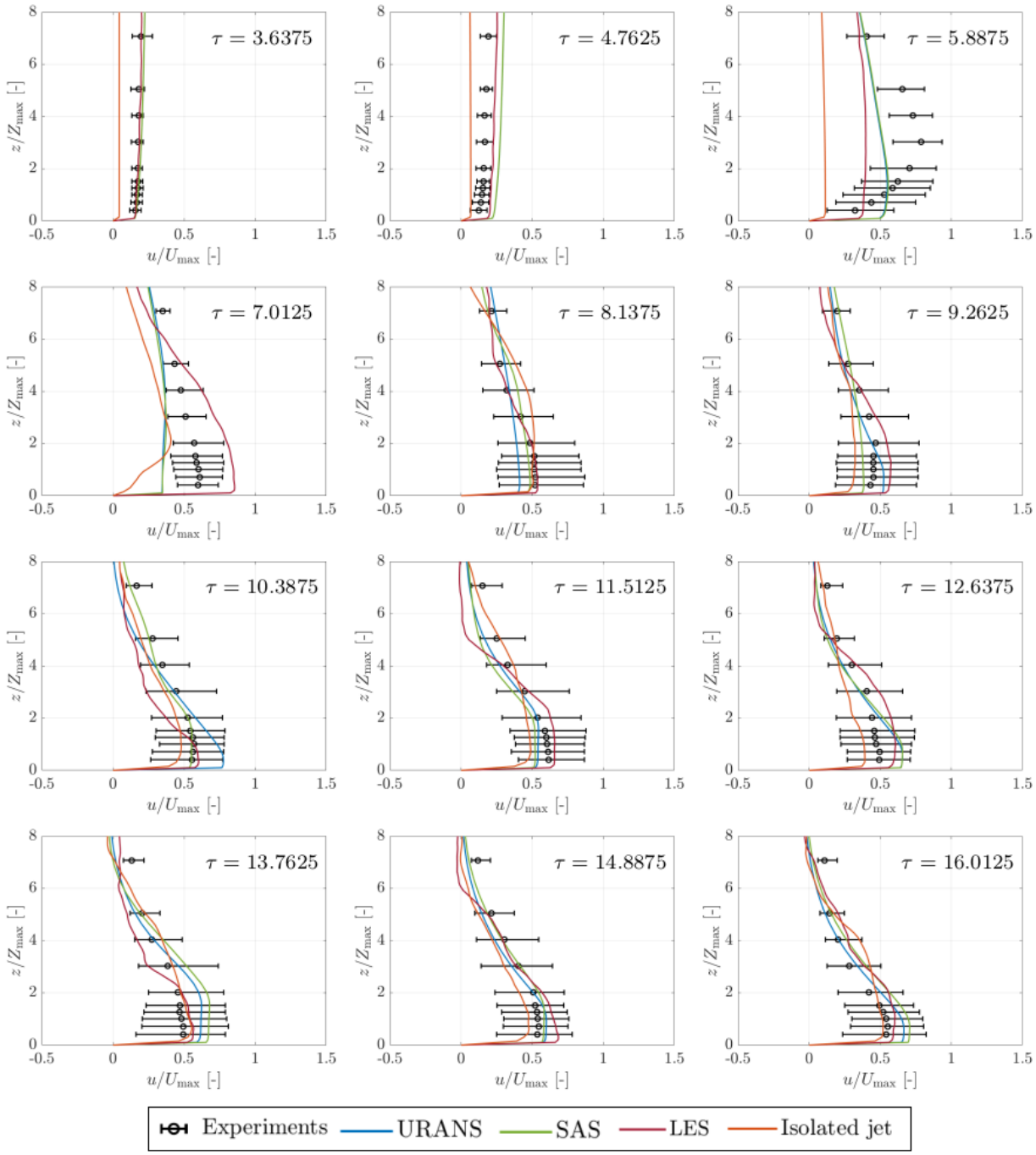

Figure 4. Comparison of measured and simulated vertical profiles of radial velocity at $\alpha = 180°$ and $R/D = 1.4$ for a selected set of non-dimensional time steps (τ).

lated downburst, while the LES once again showcased its superior behavior when compared to the URANS and SAS. In particular, LES showed a consistent and high degree of accuracy in predicting wind velocities regardless of the azimuthal location. In the perspective of importance of downburst winds for structural safety in thunderstorm-prone regions, the future work will be directed towards the CFD reconstruction of full-scale downburst events instead of focusing on reduced-scale experimental campaigns. Therefore, the selected full-scale downburst event recorded in a complex urban environment will be reconstructed in order to firstly validate the applicability of the commonly used impinging jet model, and finally to obtain its full-field flow features and its characteristics at larger scales.

References

[1] T. T. Fujita. “Tornadoes and Downbursts in the Context of Generalized Planetary Scales”. In: *Journal of the Atmospheric Sciences* 38.8 (1981), pp. 1511–1534.

[2] H. Hangan et al. “Novel techniques in wind engineering”. In: *Journal of Wind Engineering and Industrial Aerodynamics* 171 (2017), pp. 12–33.

[3] M. Hjelmfelt. “Structure and Life Cycle of Microburst Outflows Observed in Colorado”. In: *Journal of Applied Meteorology* 27 (1988), pp. 900–927.

[4] H. Kröger and N. Kornev. “Generation of divergence free synthetic inflow turbulence with arbitrary anisotropy”. In: *Computers and Fluids* 165 (2018), pp. 78–88.

[5] C. Meneveau, T. Lund, and W. Cabot. “A Lagrangian dynamic subgrid-scale model of turbulence”. In: *Journal of Fluid Mechanics* 319 (1996), pp. 353–385.

[6] R. Poletto, T. Craft, and A. Revell. “A new divergence free synthetic eddy method for the reproduction of inlet flow conditions for LES flow”. In: *Turbulence and combustion* 91.3 (2013), pp. 519–539.

[7] F. Ricciardelli. “Towards the Second Generation Eurocodes: the role of research in the updating of wind loading codes”. In: *Keynote lecture of the In-Vento 2022: 16th Conference of the Italian Association for Wind Engineering* (4 – 7 September 2022, Milano, Italy).

[8] G. Solari, M. Burlando, and M. P. Repetto. “Detection, simulation, modelling and loading of thunderstorm outflows to design wind-safer and cost-efficient structures”. In: *Journal of Wind Engineering and Industrial Aerodynamics* 200 (2020), pp. 104–142.

[9] T. Stathopoulos and H. Alrawashdeh. “Wind loads on buildings: A code of practice perspective”. In: *Journal of Wind Engineering and Industrial Aerodynamics* 206 (2020), p. 104338.

[10] THUNDERR. URL: http://www.thunderr.eu. Accessed: October 10, 2022.

Investigation of Vortex Induced Vibrations through full-scale and wind tunnel experiments

Francesca Lupi[1,2*], Ika Kurniawati[1], Hans-Jürgen Niemann[1,2], Rüdiger Höffer[1,2]

[1]*Faculty of Civil and Environmental Engineering, Ruhr-Universität Bochum, Bochum, Germany*
[2]*Niemann Ingenieure GbR, Bochum, Germany*
[*]**Corresponding author**: Francesca.lupi@rub.de

Abstract

This work investigates vortex induced vibrations by means of full-scale and wind tunnel experiments. Field measurements include wind pressures and response of wind turbine towers in real environment at the test center in Østerild, Denmark. Wind tunnel experiments are performed at the WISt wind tunnel of the Ruhr-Universität Bochum. The aeroelastic interaction in vortex induced vibrations is modelled through negative aerodynamic damping. This can be measured through wind tunnel experiments in forced vibration and is related to the phase shift between the system response and the imposed oscillation.

1. Introduction

Slender structures subjected to vortex-induced vibrations (VIV) experience an aeroelastic interaction in the lock-in range. In this study, vortex induced vibrations are investigated by means of full-scale and wind tunnel experiments. Full-scale measurements are available for two wind turbine towers of Siemens Gamesa Renewable Energy at the Test Center in Østerild, Denmark. The investigation is still on-going. While real-world conditions allow the effects of real wind profiles on lock-in mechanisms to be explored, wind tunnel experiments, on the other hand, allow the phenomenon to be studied under controlled conditions. It is found that modelling of aerodynamic damping has a relevant effect on the prediction of vortex-induced vibrations.

2. Full-scale measurements

Insight into the phenomenon of vortex-induced vibrations in the transcritical Reynolds number range is gained from pressure and response measurements of Siemens Gamesa Renewable Energy's wind turbine towers located at the Østerild (Denmark) test center.

Considering the value of the relative surface roughness of the tower surface (k/D ≈ 10^{-6}), these towers can be classified as aerodynamically smooth.

One of the challenges of field experiments for interpreting wind effects on structures is the accurate knowledge of the real environment. To this purpose, wind data from two met masts and a lidar are used in this project. In addition, an iterative procedure is developed to derive and verify the actual velocity pressure at the tower through an in-depth analysis of the pressure coefficients (see [1], [2], Figure 1).

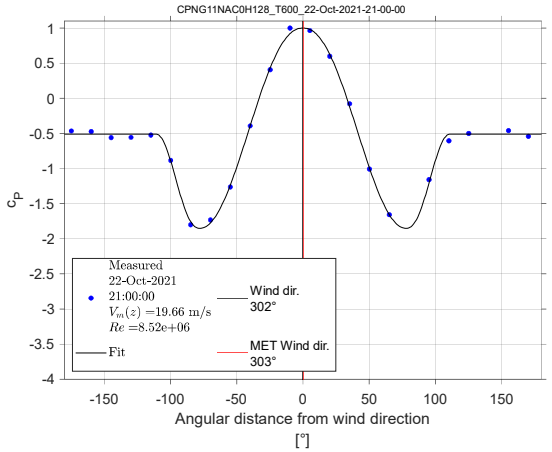

Figure 1. 10-min mean pressure coefficients.

3. Wind tunnel tests

Wind tunnel tests are performed at the WISt wind tunnel at the Ruhr-Universität Bochum (Germany).

Three different techniques are applied: (1) two-dimensional tests on an elastically suspended cylinder in smooth and turbulent flow; (2) three-dimensional

tests on aeroelastic cantilevered models in smooth flow and boundary layer flow; (3) forced vibration tests on two-dimensional cylinders.

Figure 2. Wind tunnel tests on an elastically suspended circular cylinder.

The wind response can be measured accurately in the first two cases. In the first case (Figure 2), displacements can be measured by laser sensors. In the second case, reaction forces and moments at the foot of the tower are measured with a force balance. However, these types of tests do not reveal information about the relationship between wind load and vortex resonance response.

An open question concerns the effect of resonance to vortex shedding, whether the response is driven only by a well-correlated load or whether there is also a load component in phase with the velocity of motion, which is thus aerodynamic damping. However, the experimental determination of aerodynamic damping is not straightforward, because only the joint effect of aerodynamic damping and structural damping can be observed in the response. Both damping contributions give components in phase with the velocity of motion, but the effect of structural damping is energy dissipation, while the effect of negative aerodynamic damping is energy acquisition. Therefore, these contributions balance each other to some extent.

Consequently, assuming we can measure the load and response simultaneously, the phase shift between the external load and response in vortex resonance and especially in the case of large oscillations is very small and approaches zero for large resonant oscillations. An additional difficulty is the nonlinear viscous type of structural damping, i.e., amplitude-dependent. When the structural damping can change nonlinearly with the amplitude of the oscillation, it is extremely difficult to identify small differences from an amount that may not remain constant as the oscillation increases.

Therefore, other experimental approaches, such as forced vibration testing, must be used to determine aerodynamic damping. Generally, the damping of the system can be evaluated through a foot excitation imposed from the outside. The phase shift between the response of the system and the imposed oscillation is related to the total damping of the system. If the phase shift can be measured accurately, the experiment can be repeated under different conditions (still air, with wind velocity close to the critical value, exactly at the critical value or far from the critical value). In all these cases the total damping of the system changes and this change can only be attributed to aerodynamic damping.

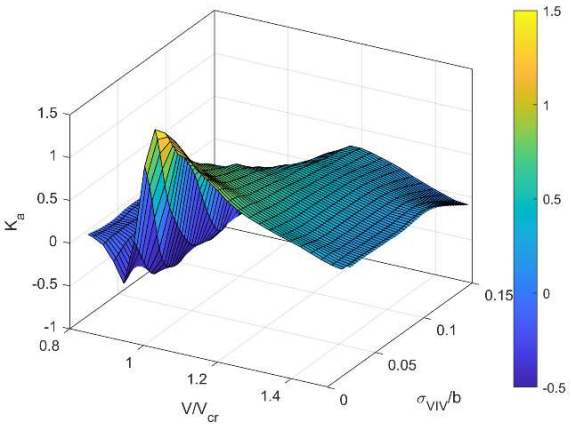

Figure 3. Negative aerodynamic damping for a circular cylinder determined through forced-vibration tests.

Figure 3 shows the aerodynamic damping in vortex induced vibrations (K_a) that is systematically measured by means of forced vibration tests (see [3], [4]). By varying the wind velocity from the critical velocity and varying the amplitude of the imposed harmonic oscillation, a three-dimensional surface can be measured discretely. Then, the three-dimensional surface can be ideally projected onto the plane (K_a, σ_{VIV}/b). The contour is a curve. This is named aerodynamic damping curve. The main feature of this experimental curve is the positive curvature.

4. Modelling

The spectral approach proposed by Vickery&Basu [5] is considered a theoretically well-founded method. The important aspect that considerably improves the prediction is the aerodynamic damping function. This

can be described in a simple way by a curve with positive curvature or in a more sophisticated way using the three-dimensional surface (Figure 3). An analytical approach based on the linearization of the generalized Van der Pol oscillator is proposed in [6].

5. Conclusions

An important discussion revolves around the question of whether vortex-induced vibrations are a force-driven response to a well-correlated load or whether there is also a load component that is in phase with the velocity of motion, namely aerodynamic damping.

This question is addressed in this study by means of full-scale and wind tunnel experiments. Full-scale investigation is still on-going.

The spectral approach proposed by Vickery&Basu is considered a theoretically well-founded method. The important aspect is the aerodynamic damping function.

6. Acknowledgements

This work is funded by the German Research Foundation (DFG – Deutsche Forschungsgemeinschaft), Project numbers 426322127 and 493357786. The authors would also like to acknowledge CICIND (International Committee for Industrial Construction) for the support through the CICIND research project “Reynolds number disparity and its effect on vortex excitation – Insight from full-scale tests at wind turbine towers”. Last but not least, we are very thankful to Siemens Gamesa Renewable Energy and Dr.-Ing. Marc Seidel for providing the full-scale measurement data and for the fruitful discussion. The supports are gratefully acknowledged.

References

[1] I. Kurniawati, F. Lupi, M. Seidel, H.-J. Niemann, R. Höffer. Field pressure measurements on a wind turbine tower in the transcritical range of Reynolds numbers. *Conference Proceedings of the 8th European-African Conference on Wind Engineering* - EACWE (2022).

[2] I. Kurniawati, F. Lupi, M. Seidel, H.-J. Niemann, R. Höffer. Insights into the transcritical Reynolds number range based on field measurements of a wind turbine tower. *Conference Proceedings of the 17th Conference on Wind Engineering* – INVENTO (2022).

[3] F. Lupi, H.-J. Niemann, R. Höffer. Aerodynamic damping model in vortex-induced vibrations for wind engineering applications. *Journal of Wind Engineering and Industrial Aerodynamics* Volume 174, 2018.

[4] F. Lupi, H.-J. Niemann, R. Höffer. Aerodynamic damping in vortex resonance from aeroelastic wind tunnel tests on a stack, *Journal of Wind Engineering and Industrial Aerodynamics*, Vol. 208, 2021.

[5] B.J. Vickery, R.I. Basu. Across-wind Vibrations of Structures of Circular Cross-section. Part I: Development of a mathematical model for two-dimensional conditions. *Journal of Wind Engineering and Industrial Aerodynamics*, Vol. 12, 1983.

[6] K. Guo, Q. Yang, Y. Tamura. Crosswind response analysis of structures with generalized Van der Pol-type aerodynamic damping by equivalent nonlinear equation method. *Journal of Wind Engineering and Industrial Aerodynamics*, Vol. 221, 2022.

Parameter identification of generalized vortex shedding model

François Rigo[1, 2, 3]*, Thomas Andrianne[1], Vincetn Denoël[3]

[1] *Wind Tunnel Lab, University of Liège, Liège, Belgium,*
[2] *FRS-FNRS, National Fund for Scientific Research, Liège, Belgium*
[3] *Structural & Stochastic Dynamics, University of Liège, Liège, Belgium*
***Corresponding author**: francois.rigo@uliege.be

Abstract
This paper proposes a generalized model for vortex shedding around a static cylinder. This model is a first step to bridge the gap between two families of Vortex Induced Vibration (VIV) models, (1) stochastic spectral models (experimentally-based) and (2) wake-oscillator models with coupled structural and fluid equations. The present model generalizes the fluid equation by combining all third-degree terms and adjusting their coefficients on experimental trajectories in phase plane. A second specificity of the proposed model stems from the observation of a non-perfectly mono-harmonic lift force envelope measured for a static cylinder in low turbulence flow. In the proposed model, stochasticity is introduced to reproduce these fluctuations, as an additive exogenous noise with Von Karman spectrum. The methodology is applied to Wind Tunnel data of a static circular cylinder in subcritical and postcritical regimes. The lift fluctuation coefficient generated with the model matches results in the literature for the considered regimes and can be adapted to other cross-section shapes.

Keywords
Vortex shedding model, Circular cylinder, Wind tunnel experimental testing, Lift coefficient, Non-linear oscillator, Wake-oscillator

1. Introduction

Different models have been proposed to study VIV and can be classified into two groups according to the number of equations (one or two) : (1) focus on the structural equation, with different ways to take into account the flow loading on the second member of the equation and (2) a coupled differential system with two variables : the structure and the wake. The study of the fluid equation in the case of a static cylinder is a first step to generalize VIV models. This was the purpose of the generalized vortex shedding model (Rigo *et al.*, 2022). When the structure is static, models that consider only the structure equation cannot simulate the fluid behaviour. Nevertheless, the model developed by (Vickery & Clark, 1972) is able to represent the fluid alone with a spectral formulation. Models (2) without structural motion simplify into one equation for the fluid. In this context, models describing the flow around static cylinders can be finally classified into two families : (1) data driven or empirical (spectrum) and (2) non-linear models such as the wake-oscillator (Hartlen & Currie, 1970; Tamura, 1981). A first objective of this model was to use generalized nonlinear terms in the fluid equation and identify them from experimental data. In the case of a static cylinder, experimental evidences show fluctuations in the lift envelope and a randomization of the generalized model is necessary. Stochasticity was introduced to reproduce these fluctuations, as an additive exogenous noise with Von Karman spectrum. This work can be seen as an effort to combine the advantages of two families of modelling : the stochasticity introduced by spectral methods and the self-limiting nature of wake-oscillator models. It is done by firstly adjusting a deterministic generalized model and secondly adding the turbulent content that allows to reproduce the fluctuations of experimental data (Method 1).

In this paper, the parameter identification of the generalized vortex shedding model is performed by adjusting all parameters (non-linear coefficients and parameters of the exogenous noise) at the same time using statistics of the measured lift force (Method 2).

This method is more robust and has the advantage of being carried out in one step. Results are compared to the procedure of Method 1 and are consistent.

For a cylinder free to oscillate (in VIV), the lift force presents also a varying envelope, the structural displacement is not perfectly mono-harmonic, especially at the start and end of the lock- in range. When only the maximal amplitude is usually computed in VIV, the displacement envelope and standard deviation can be useful when the loading is repetitive, and the structure subjected to fatigue. Such results can be predicted thanks to the generalized Vortex Induced Vibration model proposed in this paper. It is build using the generalized fluid (vortex shedding) equation from (Rigo *et al.*, 2022), coupled with a structural equation. Parameters are identified with the approach of Method 2, using statistics of both the lift force and the structural displacement. We show in this paper that the proposed model is able to accurately replicate experimental measurements. In the present paper, Methods 1 and 2 are compared using Wind Tunnel (WT) data of a static cylinder in subcritical regime. The generalized VIV model is adjusted using a WT dataset of a circular cylinder in VIV.

2. Methods

2.1 Generalized vortex shedding model

Method 1 The proposed model is presented in more details in (Rigo *et al.*, 2022) and some important elements are recalled here. This model generalizes usual non-linearities of Van der Pol, Rayleigh and energy-based equations (Hartlen & Currie, 1970; Krenk & Nielsen, 1999; Tamura, 1981), using four coefficients,

$$\begin{aligned} \ddot{q}+q &= F(q,\dot{q})+\eta \\ &= \dot{q}(\alpha q^2+\beta q\dot{q}+\gamma\dot{q}^2+\delta)+\eta \end{aligned} \tag{1}$$

where $q = 2C_L/C_{L0}$ represents a scaled lift coefficient and η is the exogenous noise (introduced in a second step). The identification method is based on a phase portrait analysis of the observed lift. It consists in adjusting coefficients $\pi = (\alpha,\beta,\gamma,\delta)$ from experimental measurements of the fluid variable : (1) by computing $\dot{q}$ and $\ddot{q}$ using finite differences and (2) adjusting the polynomial surface $F(q,\dot{q})$ on experimental trajectories to identify model coefficients using a least-square fitting procedure (Fig. 1). A harmonic balance procedure showed that β does not contribute to the amplitude of the limit cycle and therefore is chosen as $\beta = 0$. A stability analysis added another constraint for a known amplitude of the limit cycle. The optimization problem is solved for α,γ,δ under the constraints: $\delta = -(\alpha+3\gamma) > 0$.

Fluctuations in the lift envelope and the residual on Fig. 2 suggested to force this nonlinear system by exogenous noise; the proposed modelling option differs from many of the existing solutions to include incoming turbulence but as an additive forcing noise in the equation because of the signature of a wake turbulence. Among several stochastic excitations, the Von Karman spectrum was found to best approach the experimental results,

$$\Phi_\eta(\omega) = \sigma_\eta^2 \frac{2L_\eta}{\pi U_\infty}\left(1+\left(1.339L_\eta\frac{\omega}{U_\infty}\right)^2\right)^{-\frac{5}{6}} \tag{2}$$

where parameters (σ_η, L_η) are selected to adjust the model lift envelope to the experimental one.

Method 2 This method is based on the generalized model (Eq. (1) and (2)) but the identification is performed on the five parameters at the same time $\pi = (\alpha,\gamma,\delta,\sigma_\eta,L_\eta)$. The optimization problem consists in minimizing the objective function, based on four statistics of the lift force: Probability Density Function (PDF) and Power Spectral Density (PSD) of the lift force and its envelope,

$$\begin{aligned} F(\pi) = \sum_i & w_1(P(q_i,\pi)-P^*_{q,i})^2 + w_2(P(q_{e_i},\pi)-P^*_{q_e,i})^2 \\ & + w_3(S(q_i,\pi)-S^*_{q,i})^2 + w_4(S(q_{e_i},\pi)-S^*_{q_e,i})^2 \end{aligned} \tag{3}$$

where $P_{q,i}$ is the PDF of the experimental lift force, $P(q_{e_i},\pi)$ the PDF of the lift envelope from the generalized model at parameters π, i is the number of points in the PDF and j in the PSD (noted S). The weights w_i are chosen by normalizing the associated statistics. Parameters are then obtained by solving $\hat{\pi} = \underset{\pi}{\operatorname{argmin}}\, F(\pi)$ under the constraint $\delta = -(\alpha+3\gamma) > 0$.

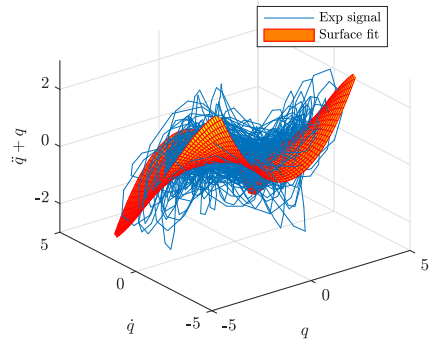

Figure 1. Experimental trajectories $\ddot{q}+q$ and deterministic polynomial surface fitting of $F(q,\dot{q})$ in phase spaces

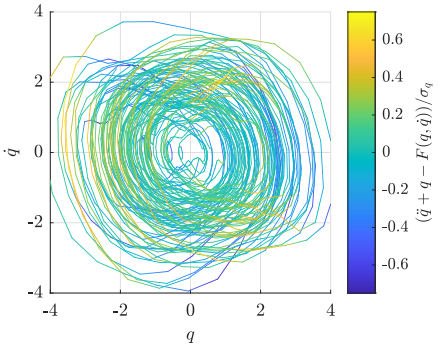

Figure 2. Residual between experimental trajectories of Figure 1 and deterministic fitted surface

2.2 Extension to vortex-induced vibration

The generalized vortex shedding model is used as the fluid equation in the generalized VIV model. The structural equation is added as a mass-damper oscillator that includes an aerodynamic damping term as a parameter to identify. The coupling between fluid and structure equations appears as an excitation in right hand-sides, proportional to q and $\ddot{Y}$ as suggested by wake-oscillator models (Tamura, 1981; Facchinetti *et al.*, 2004),

$$\begin{aligned} \ddot{Y} + (2\xi/\Omega + \xi_a)\dot{Y} + Y/\Omega^2 &= A_1 q \\ \ddot{q} - \dot{q}(\alpha q^2 + \gamma \dot{q}^2 + \delta) + q &= A_2 \ddot{Y} + \eta \end{aligned} \tag{4}$$

where $Y = y/D$ is the non-dimensional structural displacement, D the cylinder diameter, ξ the structural damping ratio, $\Omega = \omega_f/\omega_s = USt/fD$ the ratio of fluid to structure frequency, U is the fluid velocity, $St = 0.2$ the Strouhal number and f is the natural frequency. The identification procedure is similar to Method 2, by adjusting the set of parameters $\pi = (\alpha, \gamma, \delta, \sigma_\eta, L_\eta, A_1, A_2, \xi_a)$ to minimize the objective function based on statistics (PDF and PSD) of the lift force and structural displacement (similar to Eq. (3) with eight terms).

3. Results and conclusions

The WT dataset 1 was measured at the Wind Tunnel Laboratory of ULiège on a static cylinder in low turbulence flow ($I_u < 0.2\%$) in subcritical regime ($Re = 2 \cdot 10^4 - 5 \cdot 10^4$) and details can be found in (Dubois & Andrianne, 2022). On Fig.2, the proposed model (Method 1) was compared to deterministic wake- oscillator and spectral models in terms of lift dynamics and statistics (PDF of lift envelope and PSD of lift force). The exogenous noise is more suited to model wake turbulence than the white noise and results obtained with the present model match well experimental data. The fluctuating lift amplitude computed from generated signal of the model were compared to experimental data.

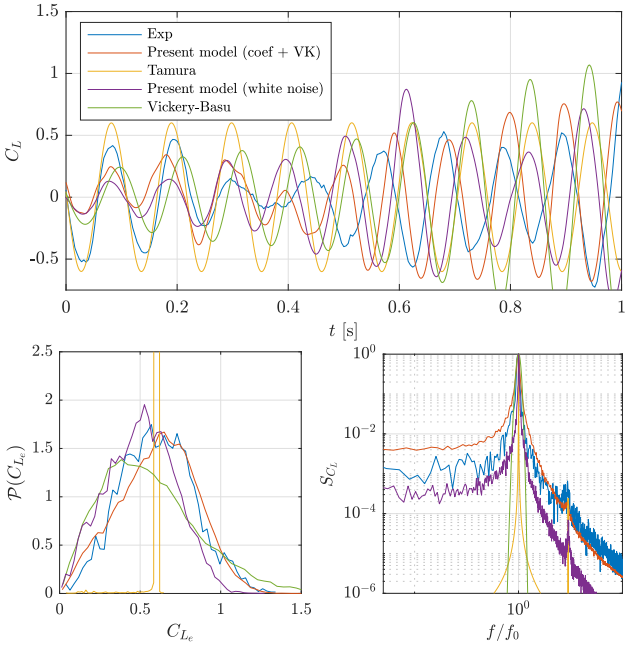

Figure 3. Comparison of models (present model with Method 1) and WT data in terms of lift force statistics, for WT dataset 1 (static cylinder at $Re = 4.5 \cdot 10^4$)

Table 1 presents parameter identification from Methods 1 and 2, leading to close results. The advantages of Method 2 are the direct identification and the robustness according to noise parameters fitting. The WT dataset 2 was measured at the WTL of ULiège on a spring-mounted circular cylinder in subcritical regime ($Re = 1 \cdot 10^4 - 4 \cdot 10^4$) with $D = 0.1$ m, $f = 7$ Hz and $\xi = 0.1\%$.

Method	α	γ	δ	σ_η	L_η
1	-0.085	0.009	0.057	0.55	1.15
2	-0.091	0.01	0.061	0.68	1.28

Table 1. Comparison of Methods 1 and 2 for the parameter identification of the generalized vortex shedding model, for WT dataset 1 (static cylinder at $Re = 4.5 \cdot 10^4$)

On Fig. 4, the generalized VIV model results at $\Omega = 1.07$ are compared with WT data. The model is able to reproduce correctly the statistics thanks to the adjustment of non-linear, additive noise and coupling terms $\pi = (-0.01, 0.09, 0.06, 0.87, 1.14, 0.002, 12, 0.004)$. Moreover, the parameters can be used in a prediction phase because their values are very close to those for the static cylinder. This work opens several perspectives. Among others, it offers a simple and robust way to identify nonlinear coefficients in the vortex shedding model for a static (and free vibration) circular

cylinder, together with the additive noise intensity and characteristic time. Static cylinders arranged in tandem configuration could benefit from this type of model. Finally, by doubling the two-equations system, the extension to flexible cylinders in tandem arrangement is also possible.

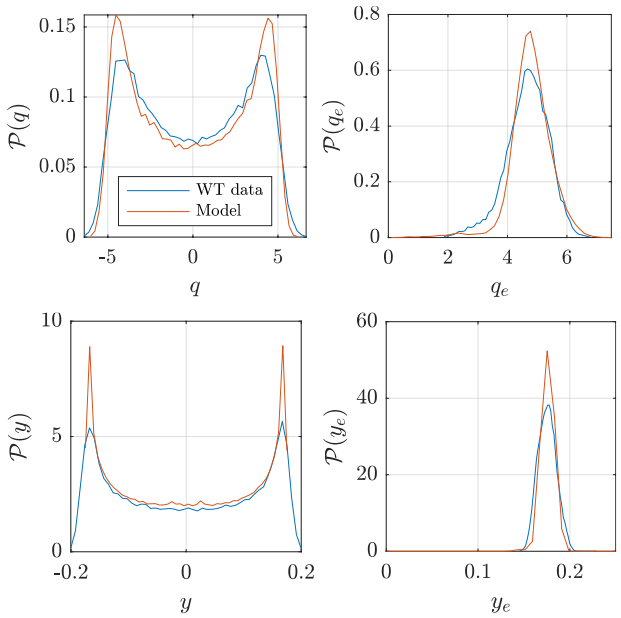

Figure 4. Results of the generalized VIV model identification: PDFs of q, q_e, y, y_e (WT dataset 2 at $\Omega = 1.07$)

Acknowledgements

This study was made possible thanks to the support of the National Fund for Scientific Research of Belgium.

References

Dubois, Rapha, & Andrianne, Thomas. 2022. Flow around tandem rough cylinders: Effects of spacing and flow regimes. *Journal of Fluids and Structures*, **109**, 103465.

Facchinetti, M., de Langre, E., & Biolley, F. 2004. Coupling of structure and wake oscillators in vortex-induced vibrations. *Journal of Fluids and Structures*, **19**(02), 123–140.

Hartlen, R. T., & Currie, I.G. 1970. Lift-oscillator model of vortex-induced vibration. *Journal of the Engineering Mechanics Division*, **96**, 577–591.

Krenk, S., & Nielsen, S. R.K. 1999. Energy balanced double oscillator model for vortex-induced vibrations. *Journal of Engineering Mechanics*, **125**, 263–235.

Rigo, François, Andrianne, Thomas, & Denoël, Vincent. 2022. Generalized lift force model under vortex shedding. *Journal of Fluids and Structures*, **115**, 103758.

Tamura, Y. 1981. Wake-Oscillator Model of Vortex-Induced Oscillation of Circular Cylinder. *Journal of Wind Engineering*, **1981**(10), 13–24.

Vickery, Barry J., & Clark, Arthur W. 1972. Lift or Across-Wind Response of Tapered Stacks. *Journal of the Structural Division*, **98**(1), 1–20.

Bayesian spectral density approach for identification of bridge section's flutter derivatives

Wei Cui[1]*, Xiaolei Chu[1], Lin Zhao[1], Yaojun Ge[1]

[1] *Department of Bridge Engineering, Tongji University, Shanghai, China*
***Corresponding author**: cuiwei@tongji.edu.cn

Abstract
This study presents a Bayesian spectral density approach for identification of flutter derivatives of bridge sections utilizing buffeting displacement responses, where the wind tunnel test is conducted in turbulent flow. Different from traditional time-domain approaches (e.g., least square method and stochastic subspace identification), the newly-proposed approach is operated in frequency domain. Based on the affine invariant ensemble sampler algorithm, Markov chain Monte-Carlo sampling is employed to accomplish the Bayesian inference. The probability density function of flutter derivatives is modeled based on complex Wishart distribution, where probability serves as the measure. By the Bayesian spectral density approach, the most probable values and corresponding posterior distributions (determined by conditions of measured signals) of each flutter derivative can be obtained at the same time. Firstly, numerical simulations are conducted and the identified results are accurate. Secondly, thin plate model, flutter derivatives of which have theoretical solutions, is chosen to be tested in turbulent flow for the sake of verification. The identified results of thin plate model are consistent with the theoretical solutions. Thirdly, the center-slotted girder model, which is widely-utilized long-span bridge sections in current engineering practice, is employed to investigate the applicability of the proposed approach on a general bridge section. For the center-slotted girder model, the flutter derivatives are also extracted by least square method in uniform flow to cross validate the newly-proposed approach. The identified results by two different approaches are compatible.

Keywords
Bayesian spectral density approach, Flutter derivatives, Complex Wishart distribution, Wind tunnel test, Bayesian inference Markov chain Monte-Carlo sampling

1. Introduction

Flutter derivatives (FDs) are of vital importance for long-span bridges, which are employed to estimate the flutter critical wind speed [5, 2] and buffeting responses [8]. Conventionally, there are two popular identification schemes to extract FDs in the wind tunnel test. The first one is achieved by a forced vibration test, where the bridge sectional model is assumed to be rigid and supported by a machine (which can move as the predefined displacement's time series) [6, 7]. The second one is by free vibration test, where the bridge sectional model is suspended by springs to move in vertical, torsional, and even lateral directions [8]. Two schemes mentioned above are both time-domain methods. This paper employs Bayesian spectral density approach [9] to extract FDs in turbulent flow utilizing buffeting displacement responses, where the affine invariant ensemble sampler (AIES) MCMC [3] is used to obtain the posterior PDFs of FDs.

2. Bayesian spectral density formulation

In the wind tunnel test, a bridge sectional model with two degree-of-freedom (DOF), i.e., h (vertical motion) and α (torsional motion), is often utilized. The dynamic behavior of the sectional model in turbulent flow can be described by the following differential equations [8]:

$$m\left[\ddot{h}(t)+2\xi_h\omega_h\dot{h}(t)+\omega_h^2 h(t)\right]=L_{se}(t)+L_b(t) \quad \text{(1a)}$$

$$I\left[\ddot{\alpha}(t)+2\xi_\alpha\omega_\alpha\dot{\alpha}(t)+\omega_\alpha^2\alpha(t)\right]=M_{se}(t)+M_b(t) \quad \text{(1b)}$$

where m and I are the mass and the mass moment of inertia of the deck per unit span, respectively; ω_i is the natural circular frequency, ξ_i is the damping ratio ($i = h, \alpha$); L_{se} and M_{se} are the self-excited lift and moment forces, respectively; L_b and M_b are the buffeting lift and moment forces due to turbulence with zero means.

The buffeting lift and moment forces can be defined as [8]:

$$L_b(t) = \frac{1}{2}\rho U^2 B\left[2C_L\frac{u(t)}{U}\chi_L + \left(C_L' + C_D\right)\frac{w(t)}{U}\chi_L\right] \tag{2a}$$

$$M_b(t) = \frac{1}{2}\rho U^2 B^2\left[2C_M\frac{u(t)}{U}\chi_M + \left(C_M'\right)\frac{w(t)}{U}\chi_M\right] \tag{2b}$$

where C_L, C_D, and C_M are the steady aerodynamic force coefficients; $C_L^{'}$ and $C_M^{'}$ are the derivatives of C_L and C_M with respect to the angle of attack, respectively; $u(t)$ and $w(t)$ are the longitudinal and vertical fluctuations of the wind speed, respectively, with zero means; χ_L and χ_M are the lift and moment aerodynamic admittances of the bridge deck, which are functions of frequency.

Denote the buffeting displacement response as $x(t) = [h(t), \alpha(t)]^T$ and the modified buffeting forces as $f(t) = [\frac{1}{m}L_b(t), \frac{1}{I}M_b(t)]^T$, then Eq. (1a) becomes:

$$M\ddot{x}(t) + C\dot{x}(t) + Kx(t) = f(t) \tag{3a}$$

$$M = \begin{bmatrix} 1 & 0 \\ 0 & 1 \end{bmatrix} \tag{3b}$$

$$C = \begin{bmatrix} 2\xi_h\omega_h - H_1 & -H_2 \\ -A_1 & 2\xi_\alpha\omega_\alpha - A_2 \end{bmatrix} \tag{3c}$$

$$K = \begin{bmatrix} \omega_h^2 - H_4 & -H_3 \\ -A_4 & \omega_\alpha^2 - A_3 \end{bmatrix} \tag{3d}$$

Considering that the fluctuations of wind speed $u(t)$ and $w(t)$ in Eq. (2) are random functions of time, Eq. (3) means that the bridge sectional model is a time-invariant linear system if the mean wind speed U is given. The frequency response function of the bridge sectional model is:

$$\mathrm{H}(\omega) = \left(K - \omega^2 M + \mathrm{i}\omega C\right)^{-1} \tag{4}$$

where K, M, and C are coupled stiffness matrix, mass matrix, and coupled damping matrix in Eq. (3), respectively; i is the imaginary unit; $\mathrm{H}(\omega)$ is the frequency response function at the specific circular frequency ω.

The PSD matrix of buffeting displacement response x is:

$$\mathbf{S}_x(\omega) = \mathbf{H}(\omega)\mathbf{S}_f(\omega)\mathbf{H}^{\star}(\omega) \tag{5}$$

where $(\cdot)^{\star}$ means the conjugate transpose of $(\cdot)$; $\mathrm{S}_f(\omega) = \mathrm{diag}\left[\mathrm{S}_L(\omega), \mathrm{S}_M(\omega)\right]$ means the PSD matrix of the modified buffeting lift force ($\frac{1}{m}L_b$) and modified moment force ($\frac{1}{I}M_b$) at circular frequency ω, respectively. Theoretically, $S_L(\omega)$ and $S_M(\omega)$ are not constant in the entire frequency band [4]. Also, the cross-spectrum of buffeting lift force and buffeting moment force is complicated [4], which is not considered in this study. This study finds that within a narrow frequency band $\mathscr{K} = \{k_1\Delta\omega, (k_1+1)\Delta\omega, \ldots, k_2\Delta\omega\}$ $(0 < k_1 < k_2)$ around the bridge sectional model's resonant circular frequency (i.e., ω_h and ω_α), the cross-spectrum of buffeting lift and moment forces can be neglected and $\mathbf{S}_f(\mathscr{K})$ can be considered as a constant matrix, which will not significantly influence the identification accuracy. Constant matrix $\mathbf{S}_f(\mathscr{K})$ can simplify the modeling procedure. The remaining formulation are omitted here for brevity and can be found in [1].

3. Wind tunnel tests

To evaluate the feasibility of Bayesian spectral density approach in extracting FDs of bridge sectional model in turbulent flow, the wind tunnel tests of a streamlined thin plate model and a center-slotted girder sectional model are carried out, respectively. The thin plate is employed because there are theoretical solutions, i.e., Theodorsen functions, of this shape. The center-slotted girder section is employed because this kind of cross sectional shape is widely utilized in current engineering practice for the construction of long-span bridges. The wind tunnel tests are carried out in TJ-1 wind tunnel at Tongji University in China. TJ-1 is an open straight-through-type boundary layer wind tunnel with a working section of 1.8 m(width)×1.8 m(height), and the wind speed can be continuously operated within the range of $0.5 \sim 25$ m/s.

3.1 Case 1: thin plate model

The FDs of a thin plate can be derived theoretically (i.e., Theodorsen function). As a result, a thin plate model is tested to verify the Bayesian spectral density approach.

As shown in Fig. 1a, the turbulent flow was generated by regularly-arranged grids, where the thin plate

model was suspended by eight springs. The thin plate model is centrally-symmetric with 1.745 m in the longitudinal dimension. As shown in Fig. 1b, the size of the cross section is 450 mm $\times$ 20 mm (length$\times$height). The mass is 6 kg/m; the mass moment of inertia is 0.7kg $\times$ m^2/m; the vertical modal frequency is 1.9 Hz, the vertical damping ratio is 0.004; the torsional modal frequency is 3.05 Hz, the torsional damping ratio is 0.003.

(a) Thin plate model with regularly-arranged grids

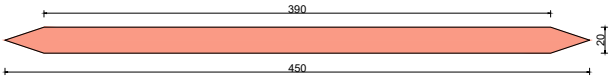

(b) Cross sectional shape of the thin plate model

Figure 1. Case 1: the thin plate model

In this subsection, we take the condition of the mean wind speed $U = 8.6$ m/s for example to explain the identification process of the thin plate. The sampling rate is 1024 Hz. Conventionally with the previous least square method in the free vibration test, the sampling duration is 10 s $\sim$ 20 s. When utilizing the buffeting response, the sampling duration is usually much longer (e.g., 14 min with stochastic subspace identification technology). In order to obtain reliable and stable measured PSDs, the sampling duration in the case of thin plate model is 2000 s, M is 8.

Fig. 2 shows that the Markov chain has converged since the autocorrelation of each parameter in θ approaches zero when lags $= 31$.

As shown in Fig. 3, for the thin plate, the FDs are approximately independent with each other in a single test. It should be stressed again that the variances shown in each posterior FD sampling, namely identification uncertainty here, are different from the experimental uncertainties examined in . The variances of each FD in this study actually stand for the posterior marginal distributions, which heavily depends on the prior information and the condition of the measured signals. We can also obtain the experimental uncertainties through the proposed Bayesian spectral density approach by statistical analysis of the FDs' MPVs in many tests with the same preset experimental

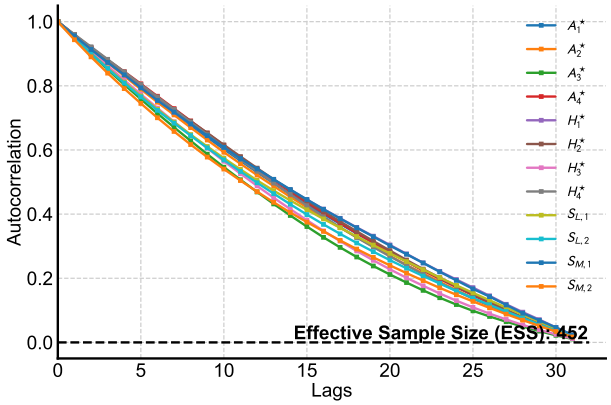

Figure 2. Case 1: MCMC autocorrelation

conditions. Furthermore, the correlation of each FD in this study is also different from that of experimental uncertainties due to the same reason.

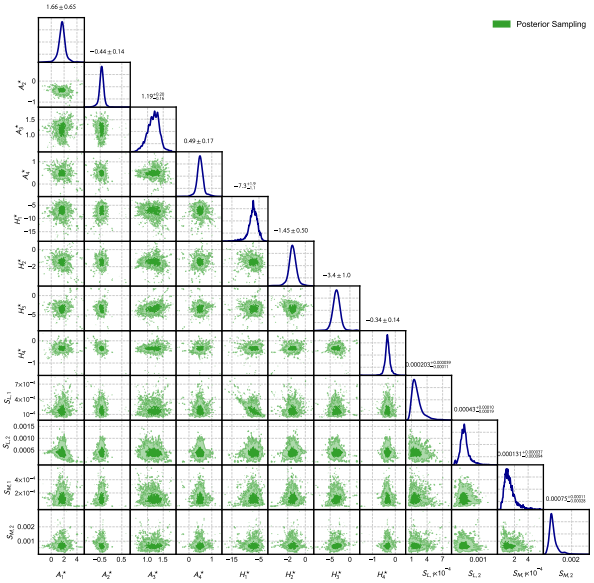

Figure 3. Case 1: posterior distributions of flutter derivatives of the thin plate when $U = 8.6$ m/s ($K_h = 0.6247$, $K_\alpha = 1.0028$)

Fig. 4 shows the posterior marginal distributions of each FD, where the 95% quantile bounds are also given. The dashed vertical line means the Theodorsen theoretical values, we can notice that the identified MPVs are generally consistent with the Theodorsen values. Some bias is observed in A_3^*, reason of which is perhaps that the thin plate is not the rigorous infinite thin plate so the "true" value is not strictly the Theodorsen solution. Similar bias can also be found.

Fig. 5 shows the reconstructed buffeting displacement PSDs with identified MPVs of FDs and buffeting force PSDs. The reconstructed PSDs are consistent with the measured ones (with $\lambda = 0.9367$), which can also prove that the identified FDs are correct. Spe-

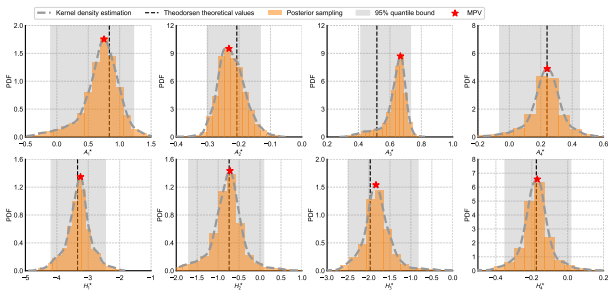

Figure 4. Case 1: posterior marginal distributions of flutter derivatives of the thin plate when $U = 8.6$ m/s ($K_h = 0.6247$, $K_\alpha = 1.0028$)

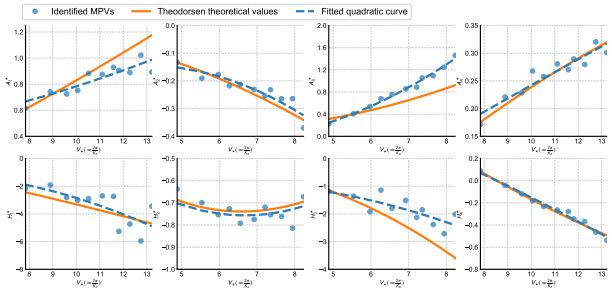

Figure 6. Case 1: identified MPVs and corresponding uncertainty of flutter derivatives of the thin plate at various reduced velocities

cially, for a general bridge cross section (i.e., there are no theoretical values of FDs for reference), one of the most efficient method to validate the identified MPVs is to reconstruct the buffeting displacement PSDs and compare those with the measured ones by using the indicator λ.

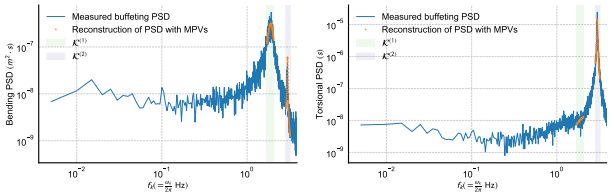

Figure 5. Case 1: measured buffeting displacement PSDs and reconstruction of PSDs with identified MPVs of FDs and buffeting force PSDs when $U = 8.6$ m/s ($K_h = 0.6247$, $K_\alpha = 1.0028$) with $\lambda = 0.9367$

Fig. 6 shows the identified MPVs of FDs at various reduced velocities. The blue dashed line is the fitted quadratic curve with identified MPVs of FDs. Generally, the identified MPVs of FDs are consistent with the Theodorsen theoretical values. Again, identified $A_3^\star$ and $H_3^\star$ are relatively higher than the Theodorsen values since the thin plate model is not perfectly infinite. Similar bias can also be found when the FDs are extracted by stochastic subspace identification technology.

3.2 Case 2: sectional model of a center-slotted girder

In order to investigate the applicability of the proposed Bayesian spectral density approach towards the general bridge cross section, we choose the widely-utilized center-slotted girder. Fig. 7 shows the cross section of the center-slotted girder. It is 1.745 m in the longitudinal dimension. The size of the cross section is 900 mm $\times$ 88 mm (length$\times$height). The mass is 11.7 kg/m; the mass moment of inertia is 1.7 kg $\times$ m^2/m; the vertical modal frequency is 1.86 Hz, the vertical damping ratio is 0.002; the torsional modal frequency is 3.00 Hz, the torsional damping ratio is 0.0015. The sampling rate is 1024 Hz. The sampling duration in the case of center-slotted girder model is 2000 s, M is 8.

(a) Center-slotted girder model with regularly-arranged grids

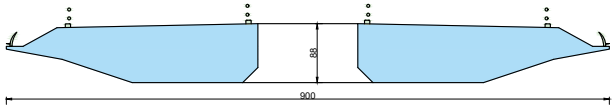

(b) Cross sectional shape of the center-slotted girder model

Figure 7. Case 2: the center-slotted girder model

In the case of center-slotted girder model, take the mean wind speed $U = 7.25$ m/s for example. Fig. 8 shows that the autocorrelation approaches zero when lags $= 27$, which means the Markov chain converges.

Fig. 9 shows the posterior samplings, where the FDs are independent with each other in a single test.

Fig. 10 shows the posterior marginal distributions of FDs, where the 95% quantile bounds are also given.

Fig. 11 shows the measured buffeting displacement PSDs and the reconstructed PSDs with identified MPVs, where a good consistency is found with $\lambda = 0.9679$. In practice, comparison between the measured PSDs and the reconstructed PSDs is of vital importance for the identification process of a general bridge section, which is an efficient method to verify the identified results.

Fig. 12 shows the identified MPVs of FDs at var-

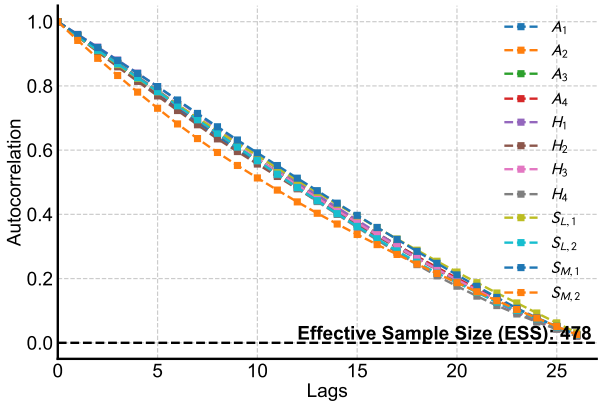

Figure 8. Case 2: MCMC autocorrelation

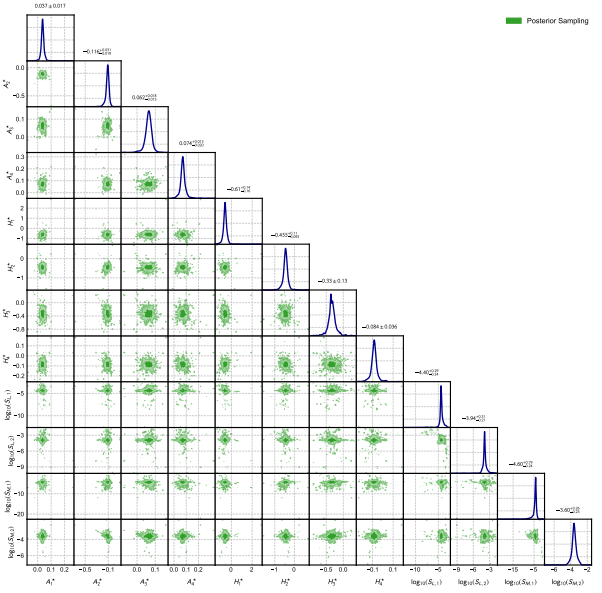

Figure 9. Case 2: posterior distributions of flutter derivatives and buffeting force PSDs of the center-slotted girder model when $U = 7.25$ m/s ($K_h = 1.4547, K_\alpha = 2.3399$)

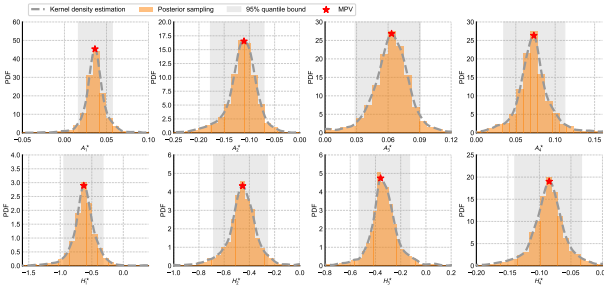

Figure 10. Case 2: posterior marginal distribution of flutter derivatives of the center-slotted girder model when $U = 7.25$ m/s ($K_h = 1.4547, K_\alpha = 2.3399$)

ious reduced velocities by the Bayesian spectral density approach in turbulent flow versus the least square method in uniform flow with free vibration data. The orange dashed lines are quadratic curves fitted by the identified MPVs at various reduced velocities of the

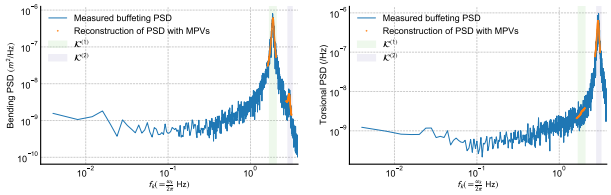

Figure 11. Case 2: measured buffeting displacement PSDs and reconstruction of PSDs with identified MPVs of FDs and buffeting force PSDs when $U = 7.25$ m/s ($K_h = 1.4547, K_\alpha = 2.3399$) with $\lambda = 0.9679$

Bayesian spectral density approach. Except $A_1^\star$, the other FDs are consistent when identified by two different methods. The latent reasons for the deviation in $A_1^\star$ need to be investigated further in the future. Anyway, the bias in $A_1^\star$ does not affect the reconstruction of buffeting displacement PSDs due to the consistency ($\lambda = 0.9679$) shown in Fig. 11. What's more, it should be noticed that at higher reduced velocity, people may also validate the identified FDs by comparison with the estimations calculated by quasi steady theory. This issue should be verified in the future if a wind tunnel, able to generate higher wind speed, is available.

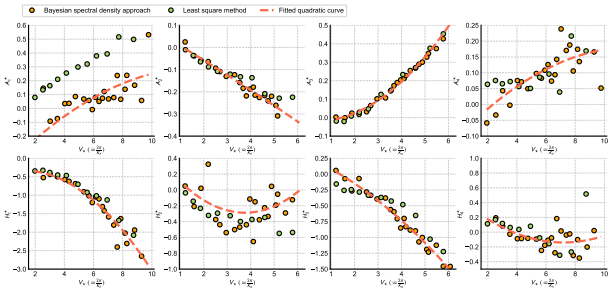

Figure 12. Case 2: identified MPVs of flutter derivatives of the center-slotted girder model at various reduced velocities by Bayesian spectral density approach in turbulent flow versus least square method in uniform flow

4. Conclusions

This paper illustrates the application of Bayesian spectral density approach on the identification of flutter derivatives, where the buffeting force PSDs can also be obtained. The identification of flutter derivatives is modeled from a probabilistic perspective based on the complex Wishart distribution. Compared with previous time-domain methods (e.g., least square method and stochastic subspace identification technology), the Bayesian spectral density approach is operated in frequency domain, which has advantages over time-domain methods. In uniform flow using free vibration, for

example, when the mean wind speed is high, the coupled damping ratio (combined action from structural damping and aerodynamic damping) will increase fast, which means that the free vibration duration is very short. Short free vibration duration can greatly influence the identification accuracy, which is the reason why the identified results at high wind speed are not reliable by least square method. However, with long enough measuring time, the statistical characteristics of buffeting displacement PSDs in frequency domain are stable and reliable. Compared with the stochastic subspace identification technology, the advantage of the frequency-domain Bayesian spectral density approach is that the frequency-domain one does not depend heavily on the assumption that the buffeting force is a white Gaussian process in the broad frequency band (as the case in the stochastic subspace identification). For Bayesian method, we only select a narrow frequency band to infer flutter derivatives, which only demands that the PSD of the buffeting force is constant at that selected narrow band. For Bayesian method, people can also easily incorporate the correlation of buffeting forces in two directions if given a theoretical model of buffeting force's cross spectrum, which is not that easy in the stochastic subspace technology. Because the grids are installed to generate the turbulent flow while conducting the wind tunnel test, the maximum of generated wind speed is relatively lower than that without grids. The advantages of the Bayesian spectral density approach are expected to be more prominent if the mean wind speed is high, which needs to be investigated in the future if a wind tunnel with more wide speed range is available. The identified results in numerical simulations, thin plate model test, and center-slotted girder model test are all satisfactory. In brief, the approach proposed in this paper offers a new angle of view (i.e., probabilistic perspective) for the inference of aerodynamic parameters in wind engineering.

References

[1] X. Chu et al. "Bayesian spectral density approach for identification of bridge section's flutter derivatives operated in turbulent flow". In: Mech Syst Signal Process 170 (2022), p. 108782.

[2] X. Chu et al. "Probabilistic flutter analysis of a long-span bridge in typhoon-prone regions considering climate change and structural deterioration". In: J. Wind Eng. Ind. Aerodyn 215 (2021), p. 104701.

[3] J. Goodman and J. Weare. "Ensemble samplers with affine invariance". In: Commun. Appl. Math. Comput. 5.1 (2010), pp. 65–80.

[4] A. Jain, N. P. Jones, and R. H. Scanlan. "Coupled flutter and buffeting analysis of long-span bridges". In: J. Struct. Eng. 122.7 (1996), pp. 716–725.

[5] X. Ji, G. Huang, and Y.-G. Zhao. "Probabilistic flutter analysis of bridge considering aerodynamic and structural parameter uncertainties". In: J. Wind Eng. Ind. Aerodyn 201 (2020), p. 104168.

[6] M. Matsumoto. "Aerodynamic damping of prisms". In: J. Wind Eng. Ind. Aerodyn 59.2-3 (1996), pp. 159–175.

[7] B. Siedziako and O. Øiseth. "An enhanced identification procedure to determine the rational functions and aerodynamic derivatives of bridge decks". In: J. Wind Eng. Ind. Aerodyn 176 (2018), pp. 131–142.

[8] E. Simiu and R. H. Scanlan. Wind effects on structures: fundar 3rd ed. New Jersey, USA: John Wiley & Sons, 1996.

[9] K.-V. Yuen and S.-C. Kuok. "Ambient interference in long-term monitoring of buildings". In: Eng. Struct. 32.8 (2010), pp. 2379–2386.

High-rise structural property identification

A.J. Bronkhorst*, D. Moretti, C.P.W. Geurts

Department of Structural Dynamics, TNO, Molengraaffsingel 8, 2629 JD Delft, the Netherlands
***Corresponding author**: okke.bronkhorst@tno.nl

Abstract

Wind-induced vibrations are an important aspect in high-rise building design. The structural properties that influence vibrations are the mass and stiffness of the building and the foundation. These properties are difficult to predict in the design, resulting in inaccurate predictions of the dynamic response. As a first step towards better predictions, this study aims to obtain accurate values of in-situ structural properties using a parameter identification technique in combination with measured modal characteristics. This study applies the technique to estimate the structural properties of a 150 m high residential tower in the Netherlands. The structural properties that were obtained for the residential tower differ significantly from the original design values.

Keywords

High-rise, wind-induced vibrations, parameter identification, modal and structural properties

1. Introduction

High-rise buildings are sensitive to wind-induced vibrations, which are therefore an important factor in the Serviceability Limit State (SLS) and Ultimate Limit State (ULS) design. The main parameters in the design calculations are the natural frequency and the damping ratio. These two parameters are difficult to estimate accurately in the design phase [1], [2] and [3]. Both parameters depend on the building mass, the building stiffness and the foundation stiffness. A better prediction of the natural frequency and damping ratio requires a better prediction of these structural properties. Information is needed on the reasons for the current mismatch between estimated and in-situ values. To obtain this information, we first need to know what the in-situ values for the structural properties are, and how these values compare to the estimated design values.

Parameter identification is a technique which uses measured modal properties to determine in-situ structural properties. This is achieved by minimizing the difference between the modal properties of a structural model and those measured on the building. The minimization problem of the difference between measured and modelled modes is posed as a constrained or unconstrained optimization. This optimization is performed using a so-called cost or loss function. The natural frequencies and mode shapes of the measurements and the model are combined in this cost function, for which the global minimum is sought in an iterative manner.

The aim of this study is the determination of the structural properties of a high-rise building using parameter identification. The technique is applied on the modal data obtained from measurements [4] on the 155 meter high residential tower ‘New Orleans’ in Rotterdam (the Netherlands).

Section 2 gives some information about the measurements on the New Orleans tower, and explains the Euler-Bernoulli beam model and the parameter identification technique. Section 3 presents and discusses the results obtained with the parameter identification. Section 4 gives conclusions and recommendations.

2. Methods

2.1 New Orleans tower

Figure 1(a) shows a picture of the New Orleans tower and its surroundings. Table 1 gives some information about the tower and the structural properties that were applied in the structural design. Since 2011, vibrations are being monitored on the 34th floor of the building, see Figure 1(d). Details about the setup of this monitoring system can be found in [3]. Additional acceleration sensors were deployed on the 15th and 44th floor for a few months to determine the

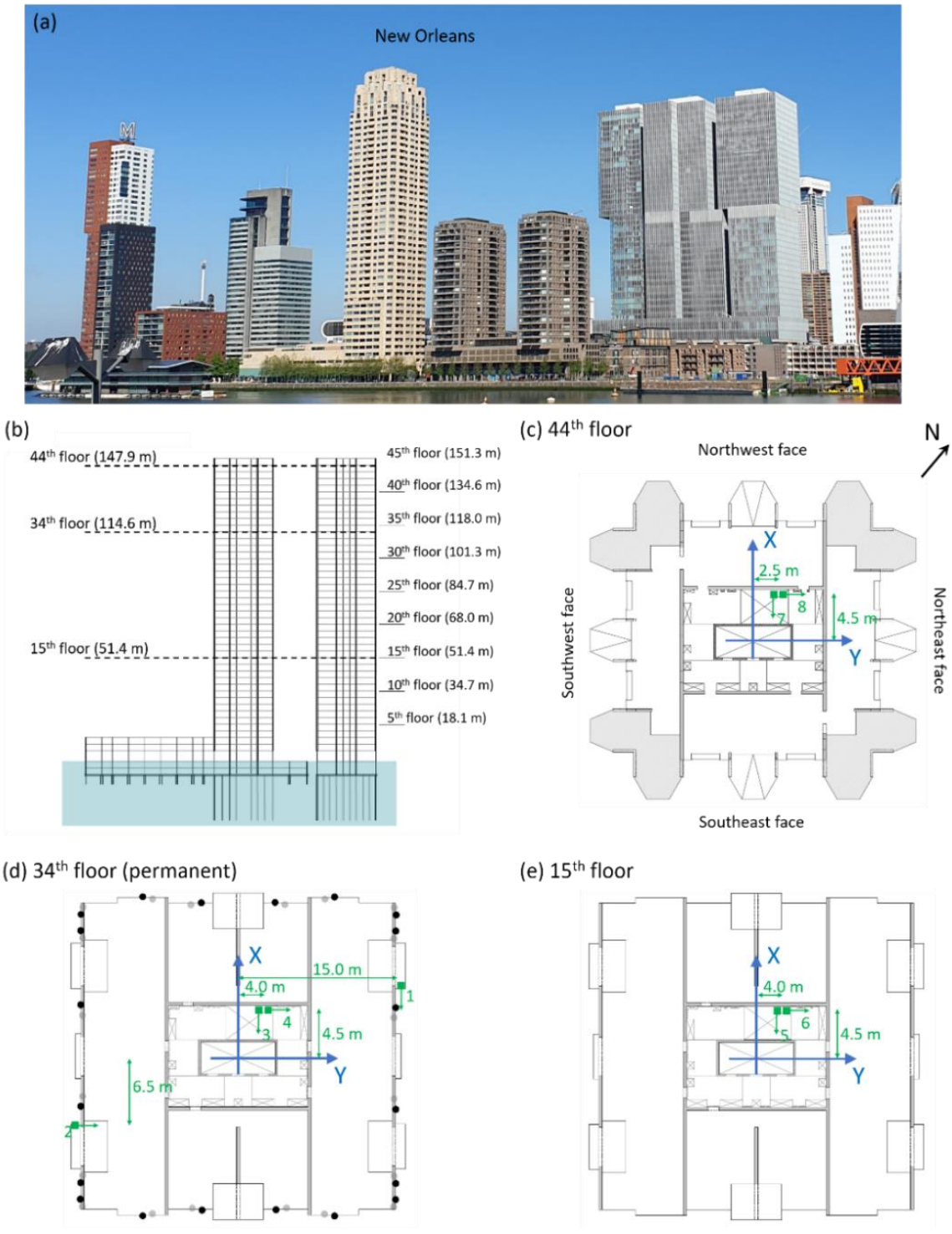

Figure 1. (a) Picture and (b, c, d and e) drawings of the New Orleans tower indicating the acceleration sensors positions (green squares) on the 15th floor, the 34th floor, and the 44th floor. The green arrows indicate the directions of the acceleration sensors. Taken from Bronkhorst et al [4].

mode shapes, see Figure 1(c) and (e). A description of the measurement setup and the application of operational modal analysis techniques to the data are described in [4].

Table 1. Structural properties applied in the design calculations of the New Orleans.

Property	Unit	Direction	
		x	y
EI	[Nm^2]	3.06E·10^{13}	2.43·10^{13}
K_r	[Nm/rad]	1.88·10^{12}	1.88E·10^{12}
K_t	[N/m]	∞	∞
M	[kg]	6.5·10^7	
H	[m]	155	
A	[m^2]	841	
ρ	[kg/m^3]	500	

2.2 Building model

The dynamic response of a high-rise building is approximated using an analytical model, which is shown in Figure 2. The model consists of an Euler-Bernoulli beam with uniformly distributed bending stiffnesses EI_x and EI_y, and a mass per unit length ρA (with ρ the building density and A the cross-sectional area). The subscript in the bending stiffness refers to the direction in which it is working (and not the axis around which it applies); so EI_x is the bending stiffness in x-direction. The foundation is modelled with rotational and translational springs in x- and y-direction ($K_{r,x}$, $K_{r,y}$, $K_{t,x}$ and $K_{t,y}$) at the base of the building model. This model applies to high-rise buildings for which bending is the dominant deformation behaviour, it does not take into account shear deformations. Furthermore, it can only be used for pure bending modes in the x- or y-direction, it does not consider torsional modes or combined bending modes.

The natural frequencies and mode shapes of this model are obtained by solving the homogeneous differential equation of motion in both x- and y-direction:

$$\rho A \frac{\partial^2 w(z,t)}{\partial t^2} + EI \frac{\partial^4 w(z,t)}{\partial t^4} = 0 \qquad (1)$$

In which $w(z,t)$ is the displacement of the beam, which is dependent on height z and time t. Using separation of variables, i.e. $w(z,t) = \phi(z)\psi(t)$, a general solution is obtained:

$$\phi(z) = A_1 \cosh(\beta z) + A_2 \sinh(\beta z) + A_3 \cos(\beta z) + A_4 \sin(\beta z) \qquad (2)$$

$$\omega^2 = \beta^4 \frac{EI}{\rho A} \qquad (3)$$

Where $\phi(z)$ is the mode shape and ω is the natural frequency. The coefficients β, A_1, A_2, A_3, A_4 are dependent on the boundary conditions. The boundary conditions for this model in x- and y-direction are:

$$EI \frac{d^2\phi(z)}{dz^2} - K_r \frac{d\phi(z)}{dz} = 0 \quad \text{for } z = 0 \qquad (4)$$

$$EI \frac{d^3\phi(z)}{dz^3} - K_t \phi(z) = 0 \quad \text{for } z = 0 \qquad (5)$$

$$\frac{d^2\phi(z)}{dz^2} = 0 \quad \text{for } z = H \qquad (6)$$

$$\frac{d^3\phi(z)}{dz^3} = 0 \quad \text{for } z = H \qquad (7)$$

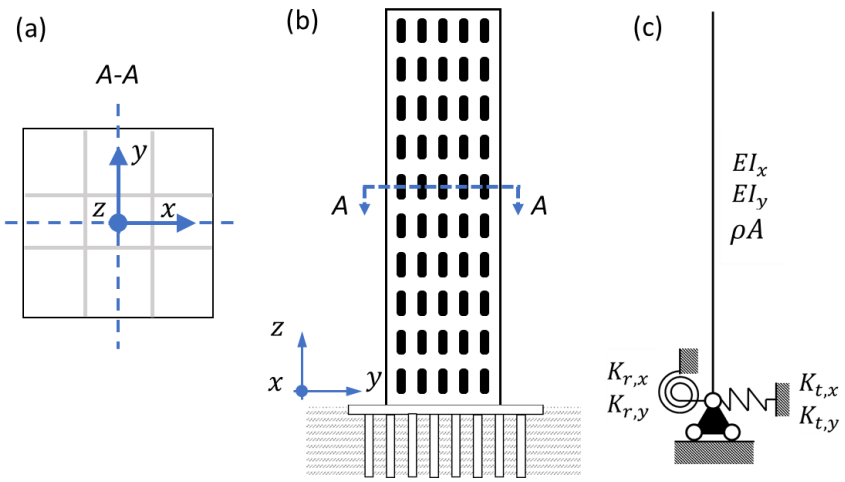

Figure 2. Schematic of a high-rise building and the beam model: (a) the building cross section, (b) side view of the building (c) Euler-Bernoulli beam model used to model the high-rise building.

Where K_r and K_t are the rotational and translational spring stiffnesses, and H is the height of the building. More information about the building model and the derivation of the coefficients can be found in [5].

2.3 Parameter identification

The modal properties of each mode i of the Euler-Bernoulli model are expressed as functions of the structural properties:

$$f_n = f\left(EI_x, K_{r,x}, K_{t,x}, EI_y, K_{r,y}, K_{t,y}, \rho\right) \quad (8)$$

$$\phi = g\left(EI_x, K_{r,x}, K_{t,x}, EI_y, K_{r,y}, K_{t,y}, \rho\right) \quad (9)$$

Where f_n and ϕ are arrays containing the natural frequencies and mode shapes in the main building axes for a certain selection of the structural properties. The functions f and g were derived with equation 2 to 7, their derivation is described in [5].

The parameter identification procedure updates the structural properties of the model to minimize the distance between the reference modal properties $\hat{f}_n$ and $\hat{\phi}$, obtained with the measured acceleration data, and the estimator modal properties f_n and ϕ. The distance is quantified using a cost function [6]:

$$J = w_f \sum_{i=1}^{N} \frac{|f_{n,i} - \hat{f}_{n,i}|}{\hat{f}_{n,i}}$$

$$+ w_\phi \sum_{i=1}^{N} \left(1 - MAC\left(\phi_i, \hat{\phi}_i\right)\right) \quad (10)$$

Where w_f and w_ϕ are weighting factors for the error contributions from the natural frequency mismatch and the mode shape mismatch; both weighting factors are taken as 1. The mode shape mismatch is quantified with the MAC (Modal Assurance Criterion) between the target mode shapes $\hat{\phi}_i$ and the mode shapes obtained with the updated structural properties ϕ_i:

$$MAC\left(\phi_i, \hat{\phi}_i\right) = \frac{|\phi_i \cdot \hat{\phi}_i|^2}{(\phi_i \cdot \phi_i)(\hat{\phi}_i \cdot \hat{\phi}_i)} \quad (11)$$

The MAC takes a value between 0 and 1, which respectively indicates no or complete similarity between the two sets of mode shapes.

The process is graphically illustrated in Figure 3 for one initial selection of structural properties. The initial selection gives a mismatch between the reference modal properties $\hat{f}_n$ and $\hat{\phi}$ and the estimated modal properties f_n and ϕ, obtained with equation 8 and 9. This mismatch is quantified with the cost function J. Based on the value and the gradient of the cost function, the structural properties are updated iteratively, thus reducing the mismatch between the reference and estimated modal properties. The optimization process is stopped when the gradient of the cost function drops below a limit value of 10^{-6}.

Due to the non-linear nature of the cost function, the obtained solution is most likely a local minimum. A different initial selection of structural properties will result in a different solution. Therefore the process is repeated for various initial selections of the structural properties, which is shown for the bending stiffness EI_x in Figure 4(a). A set of 100 initial selections is uniformly sampled within a large range of each of the structural properties to ensure the true solution is covered. The applied ranges are provided in Table 2.

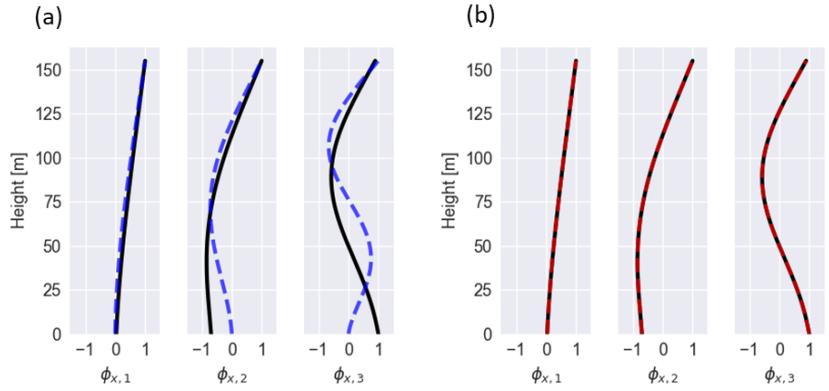

Mode	Natural frequency [Hz]		
	Actual	Start	Opt.
1	0.259	0.018	0.259
2	1.327	0.112	1.327
3	3.252	0.333	3.252

Figure 3. Optimization procedure for one selection of structural properties: (a) reference (black) and initial selection (blue) mode shapes, (b) reference (black) and optimized (red) mode shapes, (c) reference, initial and optimized natural frequencies for the three bending modes.

Table 2. Initial property bounds adopted for the parameter identification.

Property	Unit	Lower	Upper
EI	[Nm^2]	1.0 E+11	1.0 E+16
K_r	[Nm/rad]	1.0 E+10	1.0 E+15
K_t	[N/m]	1.0 E+08	1.0 E+12
ρ	[kg/m^3]	350	600

The solutions obtained with the optimization for these 100 initial selections result in a distribution of cost function values, shown in Figure 4(b). The lower quantile of these solutions, i.e. those with the smallest cost function value, are retained. New structural property ranges are defined by the 90% confidence intervals of the selected solutions, shown in Figure 4(c). Using these new refined ranges of the structural properties another selection and optimization process is carried out in the same way as the first process. This second process results in the final distribution of optimized structural properties, shown in Figure 4(d). The median and variance of this distribution are compared to the reference structural properties obtained from the measurements on the New Orleans.

3. Results

Table 3 gives the natural frequencies and MAC values for mode 1, 2, 4, 5 and 7. The design natural frequencies were determined with the building model, using the structural properties specified in Table 1. The two lowest natural frequencies applied in the SLS design calculations were actually larger (mode 1: 0.212 Hz and mode 2: 0.189 Hz). Partly due to a different calculation method for these natural frequencies, but mostly because the applicable code during the design phase of the New Orleans building, NEN 6702 [7], allows for a height correction in case of SLS design.

The measured natural frequencies of mode 1 and 2, i.e. the first bending mode in x- and y-direction, are a factor 1.7 and 1.9 higher than the design natural frequencies. The measurements indicate that mode 1 (in x-direction) has a smaller natural frequency than mode 2 (in y-direction). The natural frequencies based on the design structural properties show the opposite. This suggests that at least one of the in-situ stiffnesses (either EI or K_r) in y-direction is larger than those in x-direction, which is not the case in the design calculations (see Table 4). The natural frequencies for

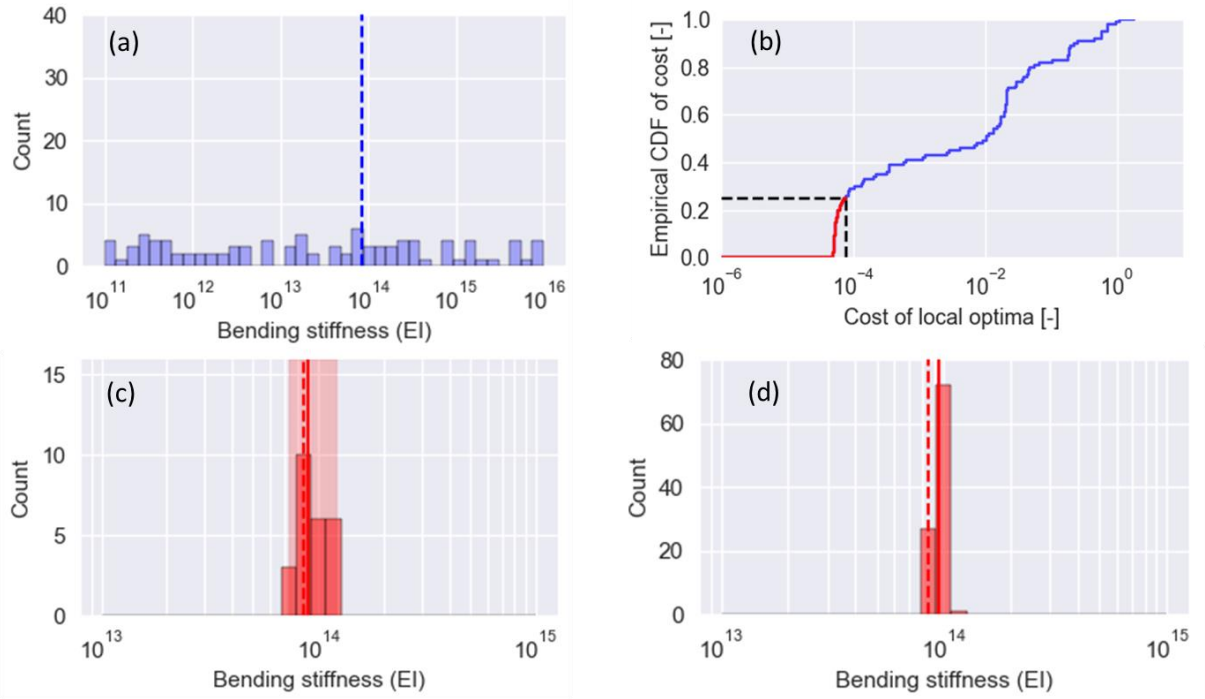

Figure 4. Procedure for multiple selections: (a) uniform sampled selections for structural properties (shown for EI_x), (b) distribution of the cost function for all local optima (blue) and selected quantile (red), (c) updated structural property range based on the 90% confidence interval (red window), and (d) final distribution of structural properties. In (a), (c) and (d) the solid line represent the median value while the dashed line is the measured value of the structural property.

Table 3. Modal properties of the New Orleans tower in terms of natural frequencies (estimated and measured) and MAC (between measured and estimated mode shapes).

Mode [-]	Natural frequency [Hz]				MAC [-]	
(dominant direction)	Design	Measured	Case 1	Case 2	Measured vs. Case 1	Measured vs. Case 2
1 (x)	0.166	0.282	0.282 ($\pm 5 \cdot 10^{-5}$)	0.286 (±0.03)	99.84%	97.58%
2 (y)	0.153	0.291	0.291 ($\pm 5 \cdot 10^{-5}$)	0.253 (±0.02)	99.73%	99.22%
4 (y)	0.989	1.332	1.332 ($\pm 5 \cdot 10^{-5}$)	1.333 (±0.04)	99.90%	98.47%
5 (x)	1.089	1.527	1.516 ($\pm 5 \cdot 10^{-5}$)	1.548 (±0.08)	99.70%	95.45%
7 (y)	2.823	2.771	-	3.111 (±0.56)	-	78.11%

the second bending mode in x- and y-direction (respectively mode 5 and 4) are about a factor 0.7 smaller than the measured values, which is relatively closer than the difference observed for mode 1 and 2. In this case, the natural frequency of mode 4 obtained with the design structural properties is smaller than that of mode 5. This is the same as observed for the measurements. Finally, the measured natural frequency for mode 7 is lower than the estimate based on the design structural properties. This comparison of natural frequencies shows that the combination of estimated structural properties in the design results in an underestimation of the natural frequencies for low modes, but in an overestimation for high modes.

The median natural frequencies obtained with the optimization procedure for Case 1 and Case 2 are close to the measured natural frequencies. Especially Case 1, with 2 modes in x- and y-direction, matches well; only mode 5 is slightly lower (less than 1%). The variation in the natural frequencies of the optimized solutions for Case 1 is also small, the standard deviation over all optimized solutions for each natural frequency is smaller than $5 \cdot 10^{-5}$. Although Case 2 gives better natural frequency estimates than those based on the design structural properties, it is not as accurate as Case 1. The MAC values also show that the mode shapes estimated by Case 2 are not predicted as well as for Case 1.

These observations indicate that the applied uniform beam model can describe the lowest two bending modes in x- and y-direction (mode 1, 2, 4, and 5) well, but that this model is too simple to accurately describe the third bending mode in y-direction (mode 7). Other modelling aspects which are not considered here, become more important for the higher modes. For example, the variation of the bending stiffness and mass over the height of the building or the frequency dependence of the foundation stiffnesses.

Figure 5 shows the distributions of the structural properties obtained for Case 1. The median values are indicated by solid lines; the design structural properties are specified with dashed lines. The corresponding values are provided in Table 4, as well as the 90% confidence bounds of the distributions. With the exception of the density ρ, the design values for the structural properties are clearly outside the ranges obtained with the parameter identification. These results provide a good first basis to determine what choices could be made in the design calculations (e.g. a higher E-modulus for concrete, or a smaller part of the variable mass) to arrive at more accurate predictions of the dynamic response.

The bending stiffness EI_x obtained with the parameter identification is larger than EI_y, which aligns with the values applied in design. It is quite surprising that both the design and parameter identification predict a larger bending stiffness in x-direction, because the first natural frequency measured in that direction is smaller than the first natural frequency in y-direction. The parameter identification results show that the larger first natural frequency in y-direction is the result of a larger rotational stiffness in that direction, i.e. the median value for $K_{r,y}$ is a factor 3.6 larger than the median value for $K_{r,x}$. The result for $K_{r,y}$ is however quite uncertain, the coefficient of variation is about a factor 6 to 7 larger than for the other structural properties.

This could indicate that the $K_{r,y}$ value obtained with parameter identification for the New Orleans is incorrect. Based on the square building planform and the almost uniform pile plan below the tower, one would expect that the rotational stiffnesses are also about the same. The results for Case 2 (with 3 modes in y-direction), suggest that for the New Orleans building the problem is related to the simplified building model with uniform stiffness over the height and no consideration of the frequency dependence of the

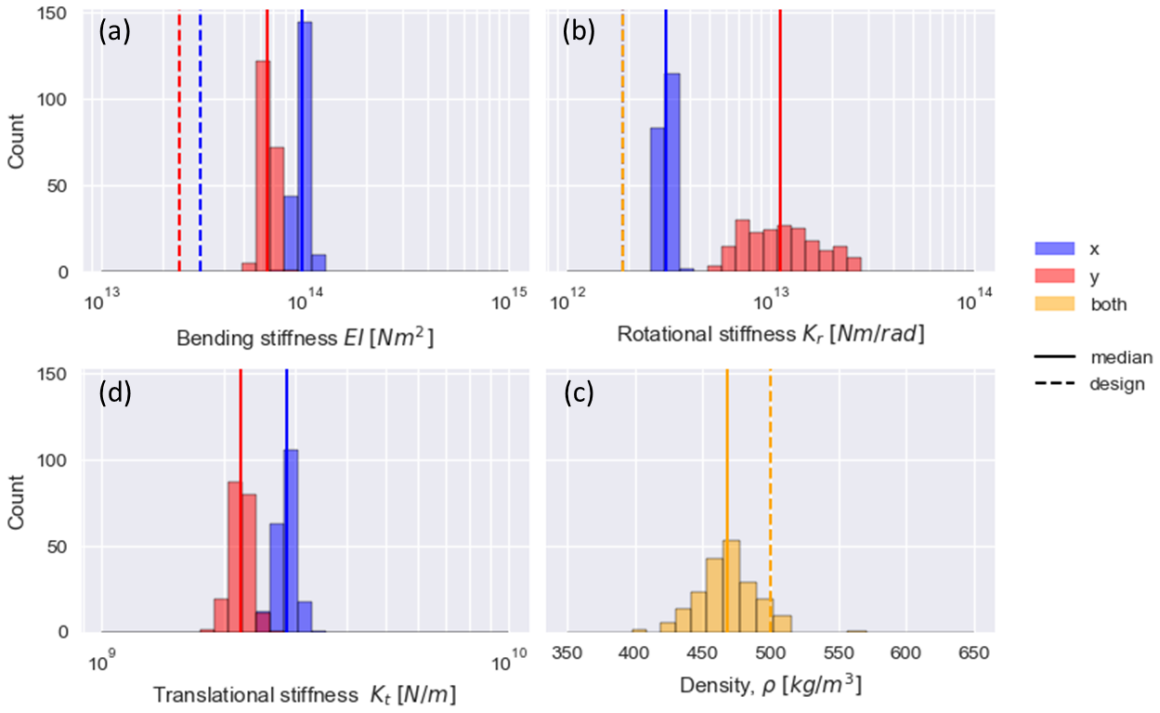

Figure 5. Distribution of the optimized properties for the New Orleans tower using 2 bending modes in x- and y-direction: (a) bending stiffness EI_x and EI_y, (b) rotational stiffness $K_{r,x}$ and $K_{r,y}$, (c) translational stiffness $K_{t,x}$ and $K_{t,y}$, and (d) building density ρ.

foundation stiffnesses. The application of a more accurate building and foundation model in the parameter identification could provide an answer to the large uncertainty in the estimate for $K_{r,y}$.

The translational stiffnesses $K_{t,x}$ and $K_{t,y}$obtained with the parameter identification are quite similar. The model used in the design calculations assumed that the building was fixed in translational direction at the base. For the first two modes, the influence of the translational stiffnesses is indeed negligible. However, for the higher modes these stiffnesses cannot be neglected. Figure 3(b) shows the significant modal displacement at the base for the second and third bending mode.

4. Conclusions

This study aimed to develop and apply a parameter identification technique for the accurate quantification of the structural properties of high-rise buildings based on in-situ acceleration measurements. The applied model is an Euler-Bernoulli beam with rotational and translational spring stiffnesses at the base. The developed technique is a two-step optimization procedure, which uses uniformly sampled starting point to cover a large part of the parameter space and allows to obtain distributions for the structural properties, thus giving insight in the uncertainty of the obtained values.

Table 4. Results of the parameter identification procedure on the New Orleans tower using 2 bending modes in x- and y-direction. For each property the median value, the 90% confidence intervals and the coefficient of variation are computed. The design values are also provided for comparison.

Property	Design	Median	Lower bound	Upper bound	COV
EI_x [Nm^2]	$3.06 \cdot 10^{13}$	$9.70 \cdot 10^{13}$	$8.62 \cdot 10^{13}$ (-11.1%)	$10.8 \cdot 10^{13}$ (+11.3%)	7.0%
$K_{r,x}$ [Nm/rad]	$1.88 \cdot 10^{12}$	$3.07 \cdot 10^{12}$	$2.76 \cdot 10^{12}$ (-10.1%)	$3.33 \cdot 10^{12}$ (+8.6%)	5.8%
$K_{t,x}$ [N/m]	∞	$2.85 \cdot 10^{9}$	$2.58 \cdot 10^{9}$ (-9.5%)	$3.07 \cdot 10^{9}$ (+7.7%)	5.4%
EI_y [Nm^2]	$2.43 \cdot 10^{13}$	$6.51 \cdot 10^{13}$	$5.78 \cdot 10^{13}$ (-11.2%)	$7.50 \cdot 10^{13}$ (+15.2%)	7.9%
$K_{r,y}$ [Nm/rad]	$1.88 \cdot 10^{12}$	$1.11 \cdot 10^{13}$	$0.64 \cdot 10^{13}$ (-42.6%)	$2.29 \cdot 10^{13}$ (+105.8%)	46.9%

Application of the technique on in-situ measurements of a residential tower showed that the structural properties differ significantly from the original design values. The obtained in-situ values for the residential tower are a first basis to determine what choices could be made in the design stage, with respect to the structural properties, to achieve more accurate predictions of the dynamic response of high-rise buildings.

Further development of the parameter identification technique could improve the accuracy of the values for the in-situ structural properties. Future work will look into the application of a more advanced building model than currently applied, to determine the large uncertainty observed for the rotational stiffness $K_{r,y}$. Furthermore, other optimization techniques will be investigated to cover the parameter space better and search the global minimum more effectively.

Acknowledgements

This work was performed in the research project "HIVIBE". The authors wish to acknowledge the participation of the partners in this research: ABT, Aronsohn, BAM, Besix, Fugro, Geobest, IMd, Peutz, SCIA Engineer, Stichting Kennisontwikkeling Windtechnologie, Structure Portante, and Zonneveld Ingenieurs. The "HIVIBE" project is financially supported by the Ministry of Economic Affairs and falls under the Topsector Water & Maritime, contract number T-DEL/2021/024.

References

[1] A.P. Jeary and B.R. Ellis, "The accuracy of mathematical models of structural dynamics. International Seminar on Dynamic Modelling," in *PD112/81*, Watford, UK, 1981.

[2] B.R. Ellis and J.D. Littler, "Lessons from dynamic testing of buildings," in *Proceedings of Structural Assessment based on full and large-scale testing*. BRE Garston, 1987.

[3] A.J. Bronkhorst and C.P.W. Geurts, "Long-term vibration and wind load monitoring on a high-rise building," in *Proceedings ISMA2020*, Leuven, Belgium, 2020.

[4] A.J. Bronkhorst, D. Moretti, C.P.W. Geurts, "Identification of the dynamic properties of the residential tower New Orleans," in *Proceedings EVACES2021*, Tokyo, 2021.

[5] M. Sonneveld, "Sensitivities and prerequisites of the application of the energy flux analysis to high-rise structures excited by wind using in situ measurements," MSc thesis, TU Delft, 2020.

[6] W. Torres, J. L. Almazán, C. Sandoval, and R. Boroschek, "Operational modal analysis and FE model updating of the Metropolitan Cathedral of Santiago, Chile," in *Engineering Structures*, 143, p. 169-188, 2017.

[7] NEN, "NEN 6702 Technical principles for building structures – TGB 1990 – Loadings and deformations," Delft, 2007.

Inverse identification of the gust loading on a high-rise tower with Bayesian statistics

Frank Kemper[1]*, Chris Geurts [2]

[1] *Center of Wind and Earthquake Engineering, RWTH Aachen University, Germany and TNO, Delft, The Netherlands*
[2] *Department of Structural Dynamics, TNO, Delft, The Netherlands*
***Corresponding author**: kemper@cwe.rwth-aachen.de*

Abstract
For the modeling of stochastic structural responses due to wind gusts, reasonable assumptions for the aerodynamic admittance are elementary. However, a large variety of corresponding models exists and lack validation and reliable model estimation studies based on real data. In this paper, full-scale data from a high-rise tower in Rotterdam is used to inversely identify the aerodynamic admittance (size-effect and joint-acceptance functions, SE, JAF) based on Maximum Likelihood Estimates (MLE), Markov-Chain Monte Carlo (MCMC) sampling and a Bayesian posterior (BP) implementation to find parametric models for both aspects of aerodynamic admittance.

Keywords
Aerodynamic Admittance, Stochastic Vibrations, Gust Response, Bayesian Parameter Modeling

1. Introduction

Modeling load composition and coherence to predict the stochastic response of slender structures realistically has been a topic of research for decades already now. Based on the initial concept by *Davenport* [1], which is based in the frequency domain for a simplified single-degree of freedom (SDOF) system, various authors have proposed enhanced concepts for more realistic descriptions of the problem. *Natke* [2] presented the identification problem and some results based on measurements. *Geurts* [3] has presented coherence surface pressure coherence based on monitoring data.

A significant source of uncertainty in the described approach is the considered spectral wind force distribution and its interference with all actual present mode shapes. The term aerodynamic admittance describes firstly a ”size-effect” (SE) i.e. the efficiency of the wind load with respect to the load-affected area. Secondly, it interferes with the dynamic load bearing behavior, leading to the ”joint-acceptance function” (JAF). For slender structures like high-rise buildings, both the SE and the JAF are of interest. An overview of procedures and analysis techniques for the JAF has been given by *Zhou* [4], pointing out that there exists a variety of aerodynamic admittance recommendations.

In this paper, monitoring data of a high-rise building in Rotterdam, the Netherlands, is used to determine models for the SE and the JAF based on Maximum Likelihood Estimation (MLE) and Bayesian posterior (BS) implementation. As data is available for a time period of more than ten years, a significant statistical deepness can be expected for a wide variety of wind directions (undisturbed and interfered with by neighboring structures).

2. Building and Measurement Data

The high-rise building ”New Orleans Tower” (NO Tower) is located in the center of Rotterdam, on a small peninsula in the river ”Nieuwe Maas.” The height is $h = 158m$, the depth and width are $d = h = 29m$, respectively. Relevant measurements comprise external pressure at the facade exterior for one horizontal section and 2D accelerations at three different heights, and an ultrasonic anemometer on top of the building. Signals are acquired with a frequency of $f_s = 20Hz$. Additionally, wind data of the nearby airport Rotterdam-The Hague (RTM) is available as hourly averages.

Figure 1. NO-Tower and surrounding in Rotterdam

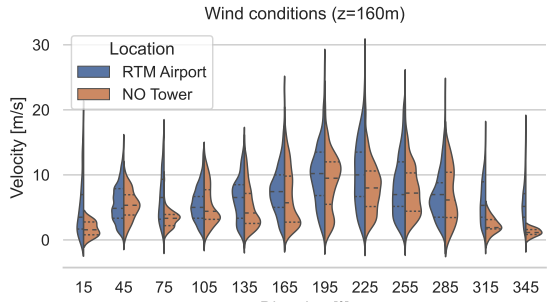

Figure 2. Probabilities of wind speed at RTM (scaled up to $z = 160m$) and NO Tower ($z = 160m$)

Due to the high sampling frequency, the data set is large and the handling needs specific access prerequisites. All data has been transferred to a SQL database allowing for fast and reliable reduction of data, e.g., according to classes of wind velocities and directions. Such filtered accessibility of all data sets is a key condition for real data analyses, especially wind engineering.

Fig. 2 shows a comparison of hourly averaged wind velocity v_m data acquired at RTM and NO Tower, whereat the available $v_{m,ROT}(z = 10m)$ was converted to $h_{NOTower} = 158m$ via an exponential law with a profile exponent $\alpha = 0.15$. The violin plot shows direction-wise probabilities of wind velocity distributions. Influences of neighboring structures and the roof of the NO Tower itself result in divergence of distributions. Otherwise, the correlation seems reasonable, confirming the suitability of the chosen exponential coefficient. Two wind directions are of special interest for the analyses: 1) $\phi_1 = 142°$, free of flow interference, 2) $\phi_2 = 232°$ with the interference of windward rectangular high-rise tower (Montevideo). Both directions are perpendicular to the building's surface. For the presented analyses, direction 1) has been chosen.

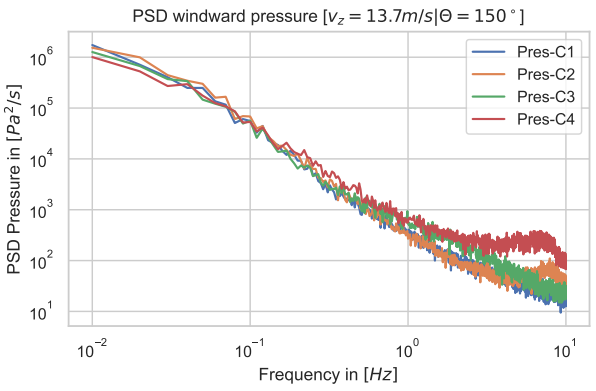

Figure 3. PSD of wind pressure of four windward pressure taps at level 34 ($z = 115m$)

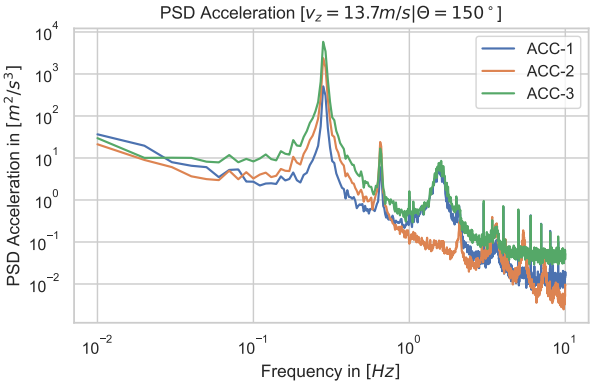

Figure 4. PSD of in-wind accelerations measured at three different heights ($z_{1,2,3} = 51m, 115m, 148m$)

3. Modeling Aerodynamic Admittance

The analysis of gust-induced responses can be performed either in the time domain or in the frequency domain. After a brief explanation of time-related effects, a frequency model is introduced, which is the base for the performed analyses.

3.1 Time based model

For high-rise structures, the time-dependent wind load f per unit length can be expressed by:

$$f(z,t) = \rho c_D(z) b(z) \bar{v}(z) v'(z,t) \tag{1}$$

whereat the velocity pressure is linearized ($v'^2 \approx 0$). The aerodynamic pressure coefficient c_D considers the load admittance of the cross-sectional part per unit length for the considered structural width.

In the time domain, the integral generalized force over the complete structure considering a relevant mode shape Φ results to:

$$F(t) = \rho \int_0^H c_D(z) b(z) \bar{v}(z) v'(z,t) \Phi(z) dz \tag{2}$$

The integration is effectively a time averaging of the active velocity components. With increasing spatial distance $\Delta_{i,j}$ or with increasing gust frequency, the correlation between two heights h_i and h_j decreases. Due to the location and frequency-dependent - and due to the stochastic character of turbulent wind - the formulation in the frequency domain is beneficial.

3.2 Frequency based model

3.2.1 Gust spectra

An important link between time and frequency-based analyses are auto- and cross-correlation functions (Wiener–Khinchin theorem). Power spectral density (PSD) functions can be used to express the decrease of correlation dependent on spatial distance in a frequency-dependent way. The components of the gust velocity

matrix $\mathbf{S_{uu}}$ are defined as:

$$S_{uu,ij}(f) = \mathrm{COH}_{ij}(f) \cdot S_{uu}(f) \tag{3}$$

For all presented analyses, instead of the gust spectrum S_{uu}, the spectrum of gust velocity pressure S_{pp} is used. The linearized relation between both is:

$$\mathbf{S_{pp}}(f) = (\rho \bar{c}_p \bar{u}) \cdot \mathbf{S_{uu}}(f) \tag{4}$$

where c_p is an aerodynamic pressure coefficient. According to [3], the assumptions behind this linearization are questionable. In 5.3 this is discussed in more detail.

3.2.2 Aerodynamic Admittance

In general, the aerodynamic admittance H_A expresses the relationship between a punctual velocity pressure p and the structural relevant force f. In the frequency domain, this is expressed as:

$$\mathbf{H_A}(f) \cdot \mathbf{S_{pp}}(f) \cdot \mathbf{H_A}(f)^T = \mathbf{S_{ff}}(f) \tag{5}$$

The term aerodynamic admittance describes the process of aerodynamic force generation due to the natural turbulent wind flow. For slender structures, the load effect can be split into a cross-sectional part and a length- or height-related part corresponding to the main dimension of the structure. A reason for splitting both parts is that the length-related part needs to be generalized over the mode shape(s) to model the admittance effect in a simplified way (e.g., for codes).

It can be distinguished, whether the load-affected structure reacts independently of the position of loading or not. The size effect describes the effect of spatial and temporal averaging of pressure on the resultant (effective) loading, independent of the load effect. The coherence function is generally important with respect to the integration of pressure over surfaces and the resulting effective loading. Based on a known force spectrum $\mathbf{S_{ff}}$. In Fig. 5, coherence analyses of four windward pressure taps are shown. With increasing spatial distance, the load correlation decreases dependent on gust frequency.

For main load-bearing systems of slender structures, the load efficiency with respect to the caused load effects is relevant, taking into account the structural properties (e.g. an influence line or a mode shape). An aerodynamic admittance function, which takes into account the load effect, is called Joint Acceptance Function (JAF).

3.2.3 Joint Acceptance Function (JAF)

As specific load effects of structure depend on the load location, the beneficial effect of load correlation (or

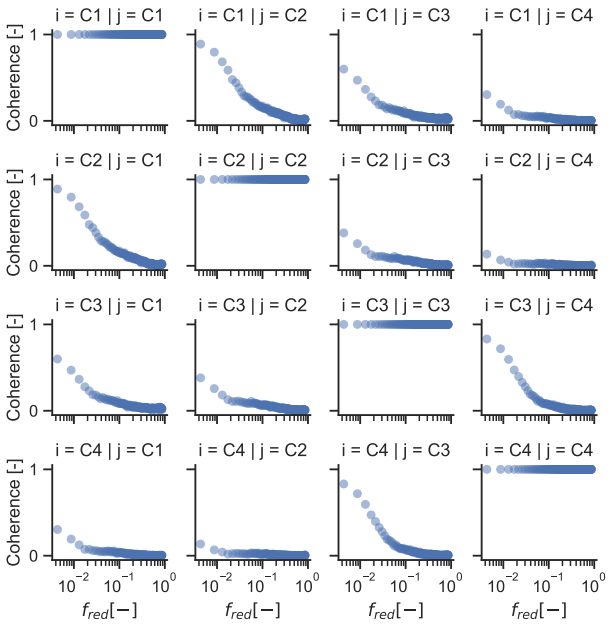

Figure 5. Pressure coherence of four windward pressure taps at level 34 ($z = 115m$)

coherence) needs to be analyzed under this premise. This is done by formulation of the joint acceptance function (JAF), which projects the coherence effects onto the dynamic properties of the considered system. The structural response r_{ij} of an MDOF system to wind loading f_{ij} is expressed in the frequency domain by:

$$\mathbf{H_M}(f) \cdot \mathbf{S_{ff}}(f) \cdot \mathbf{H_M}(f)^T = \mathbf{S_{rr}}(f) \tag{6}$$

By the application of mode decomposition, the problem can be simplified to a set of linear equations. As for the analysis vectors of acceleration are used, the impedance function (force to acceleration) as mechanical admittance function is used:

$$H_M(f) = \frac{A \cdot (f/f_0)^2}{\sqrt{[1-(f/f_0)^2]^2 + [2D(f/f_0)]^2}} \tag{7}$$

where f_0 is the natural frequency, and D is the damping ratio. The scaling factor A covers the system-dependent stiffness. For further analyses, the scaling of the spectral distributions is not considered; effects are normalized instead. For the determination of the matrix $\mathbf{H_M}$, normally finite element analysis is performed (here as displacement admittance):

$$\mathbf{H_M}(f) = \left[-(2\pi f)^2 \mathbf{M} + i2\pi f \mathbf{D} + \mathbf{K}\right]^{-1} \tag{8}$$

Equations (3) till (7) describe the well known components of the frequency based wind load model, introduced by *Davenport* [1], in a matrix based formulation. The equations are normally used in a forward mode,

with different model assumptions, and for SDOF systems. Especially the aerodynamic admittance $\mathbf{H_A}$ or the JAF are assumed based on the coherence of the wind field, see Eq. (3) and a simplified linear mode shape.

In general, data for $\mathbf{H_A}$ based on data is rare because it cannot be measured directly. Also, the spectral wind force at different levels can normally not be directly determined. Hence, it needs inverse identification concepts to use measurement data of structural response for this aim.

The main idea of inverse identification is to determine structural properties firstly and then inversely multiply the mechanical admittance $\mathbf{H_M}$ (or impedance) with the measured responses $\mathbf{S_{rr}}$ to obtain the causal wind force $\mathbf{S_{ff}}$, see Eq. (6). The ratio of the force spectrum $\mathbf{S_{ff}}$ and the spectrum of velocity pressure $\mathbf{S_{pp}}$ (estimated by a windward pressure tap) allows the identification of the desired mechanical admittance $\mathbf{H_A}$, which is a JAF for the considered mode shape, see Eq. (5).

4. Methods to solve the Inverse Problem

4.1 Solution concept

Whenever response data d shall be used to determine prior parts of the underlying process (e.g., load and mechanical transfer), uncertainties in the data ($d_{true} + \eta$) of the measured values complicate the backward prediction. Besides that, the (load) model m is based on several unknown parameters (like load position, amplitude, and correlation), which, in an ideal case, are deemed to be solved by the solution of the inverse problem. The connection between input m and output d in a forward sense is the function G (e.g., a structural model). In general, the inverse problem can be described as:

$$G(m) = d_{true} + \eta \tag{9}$$

The right part of Eq. 9 represents the measured data $d_{true} + \eta$ (here: surface pressure or accelerations). G is the physical, structural system that can be formulated as a linear complex mechanical impedance function (for known properties) or decomposed using the signals of measured vibrations. In this work, a higher-order dynamic mode decomposition (DMD) has been implemented for the goal.

Difficulties in solving inverse problems are solution existence, solution uniqueness, and the instability of the solution process (explanation, see [5]). For this reason, the solution of inverse problems is handled based on a parameter estimation (linear regression) where the likelihood of the model m parameters is maximized. In the second step, based on Bayesian posterior statistics, the quality of the model can be assessed using additional measurement data (model calibration), see 5.3.

4.2 Dynamic Mode Decompositon (DMD)

For the analyses in this study, a higher order dynamic mode decomposition [6] has been used. The main difference to a conventional DMD is the consideration of time windows and time lags, leading to a superimposed version of the DMD algorithm. In Fig. 6, the PSD an acceleration sensor on top of the NOT is shown, the decoupled modes and their sum. The decomposed mode no.1 has been highlighted as it is used for the inverse determination of the JAF.

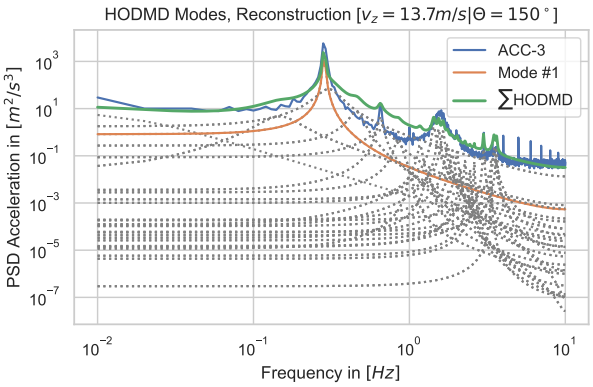

Figure 6. Mode decomposition with high order DMD and reconstruction of the PSD of sensor 3

The decomposition of the response signal is interpreted as a combination of a modal response. That means, for the highlighted mode shape #1, the associated frequency-dependent response takes place with its corresponding mode shape (1st shape in bending).

5. Model Parameter Estimation

5.1 Coherence and Size Effect (SE)

The SE for a single storey is expressed by a model of pressure coherence. Measured data and MLE, BP fitting approaches allow for a model determination with additional statistical information about the involved parameters. For the parametric model, a typical analytical expression of a spectral decay has been chosen:

$$\mathrm{COH} = \alpha \cdot \left[\exp\left(-C\,\frac{f \cdot d}{u}\right)\right] + \eta \tag{10}$$

where C is denoted as the decay parameter. As the coherence function tends to $COH \to 1$ for frequencies tending to $f \to 0$, the parameter α was chosen to allow the quality of the resulting fit. The parameter η covers

signal noise. The basis for the parameter estimation was the coherence calculations of differently grouped sets of pressure taps, see Fig. 5.

5.2 Joint Acceptance Function (JAF)

The JAF is expected as a decay function, corresponding to Eq. (10) as well. For the fitting procedure, a fixed constraint of $\alpha = 1.0$ is used because present differences in amplitude are constant factors, which are related to aerodynamic coefficients, geometry, and so on. For the analyses in this study, just the ratio of PSD amplitudes is relevant. Therefore, the JAF is normalized to 1.0 for low frequencies.

5.3 Coherence Fitting

5.3.1 Maximum Likelihood Estimation

A first parameter fitting has been done based on MLE, which allows for identifying the most likely combination of model parameters. For the identification, analyses have been made with the parameter α as a variable and a fixed constraint of $\alpha = 1$.

For the analysis, joint probability density functions are used, which are determined based on the present data sets (pressure for coherence and acceleration for JAF). As a result, the most likely set of parameters of the provided model will be returned [5].

To identify the effective spectral wind force and the spatial coherence effect, it is necessary to estimate the present gust velocity spectrum $S_{uu}(f)$. At the stagnation point, the velocity spectrum can be estimated based on pressure measurements with:

$$S_{uu}(f) = \frac{S_{pp}(f)}{\rho^2 \cdot c_p \cdot u_m} \tag{11}$$

This implies the simplified assumption that the gust velocity spectrum is identical to the pressure spectrum at the surface of the building. In fact, on the one hand, on the windward side of a building, pressure equalization takes place (stagnation region). On the other hand, the aerodynamic process is significantly superimposed by vorticity (wind parallel and leeward sides).

In [3], this was investigated and shown that the simplification is not realistic. However, for the analysis, currently, no better data source was available because the anemometer on top of the building suffers disturbances. Later, the analysis will be updated with velocity measurements of another high-rise tower in Rotterdam, whose anemometer is installed on a significantly higher mast.

5.3.2 Priors and Posteriors for Bayesian Fit

A deeper look at the modeling quality can be achieved using Bayesian statistics. As a starting point, the likelihood model can be used, which is called the prior in this case. In principle, Bayesian statistics shifts the focus from the data to the model. Based on new data, the model parameters are calibrated, which results in the posterior result. Hence, parameter likelihood is investigated is under given conditions, whereat the conditions are new sets of data. Based on this procedure, we can learn about the goodness of a model, the interdependence of parameters, and the sensitivity to new observations. The methodology is, therefore, ”self-learning.”

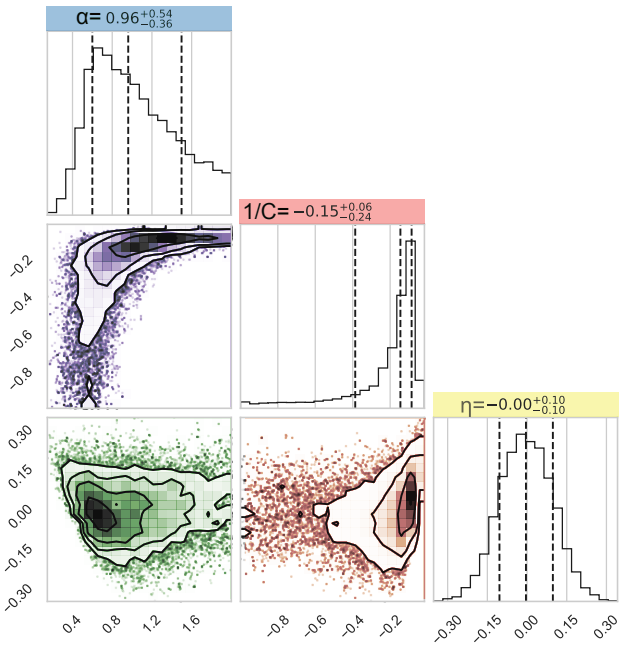

Figure 7. Posterior of Bayesian inference for the coherence model (example for pressure tap C-1)

5.3.3 MCMC Sampling

The Markov-chain Monte Carlo approach is used to unveil dependencies of model parameters and their sensitivity using synthetic data instead of measured ones. Using such sets, it is possible to determine the posterior distributions of every single parameter and crosswise considering their interference. In Fig. 7, the Bayesian posterior after MCMC is shown to model pressure coherence. As a data source, the windward pressure tap C1 have been considered.

6. Inverse Identification of the JAF

For the inverse modeling of the JAF, the following analysis steps have been carried out:

1. Computation of the averaged PSD of acceleration; see Fig. 4,
2. DMD to isolate the modal response for the frequency of interest ($f_1 = 0.28Hz$, 1st shape in bending), see Fig. 6.

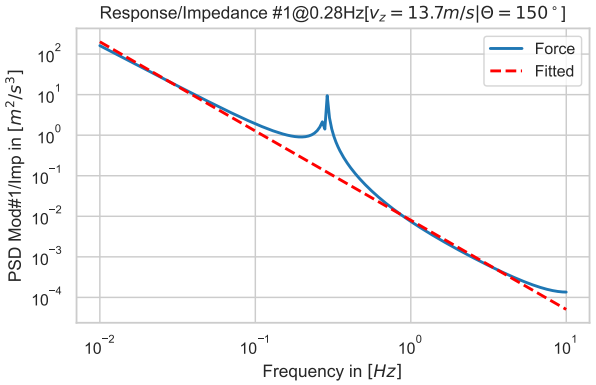

Figure 8. Aerodynamic force as the ratio of response and impedance

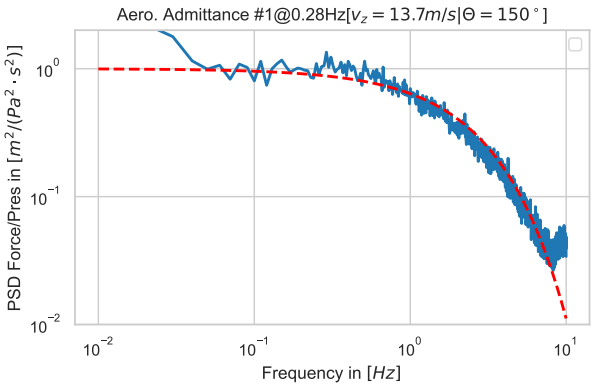

Figure 9. Inversely estimated JAF for the first mode shape of the NOT

3. Ratio of modal response to impedance function acc. to Eq. (7) results to estimated PSD of aerodynamic force, see Fig. 8. In the present analysis, this force turns out linear (disturbance at natural frequency is negligible).
4. Ratio of force and pressure PSD is JAF for the considered mode shape; see Fig. 9.
5. Model fit based on MLE enables the estimation of the resulting model; see Fig. 9, red line.

Results for the lowest frequencies can be ignored as the impedance function tends to zero for low frequencies. The slight increase of the determined JAF for frequencies close to $f = 10$Hz is explained with vorticity effects, as already visible in the spectra of pressure taps; see Fig. 3. Such an increase needs to be handled by a vortex model.

7. Conclusions

Generally, input identification is an important task in wind engineering. For this aim, the availability of high-quality data for a residential high-rise building with a time coverage of more than ten years is extremely valuable for research. In the present paper, ongoing work for identifying aerodynamic admittance is presented. In the first part of this work package, a toolset has been established. For two selected cases (SEF and JAF), results are presented for an undisturbed wind direction with a reduced time period of within 2020. The results show clearly that the recorded data sets allow for spectral analyses of aerodynamic admittance. Especially for this complex effect of wind-induced vibrations, model estimations based on real data are rare. Hence, it is aimed to consider the full range of data periods and apply the advanced model estimation techniques presented in the paper.

8. Acknowledgement

This work was performed in the HIVIBE research project. The authors wish to acknowledge the participation of the partners in this research: ABT, Aronsohn, BAM, Besix, Fugro, Geobest, IMd, Peutz, SCIA Engineer, Stichting Kennisontwikkeling Windtechnologie, Structure Portante, and Zonneveld Ingenieurs. The HIVIBE project is financially supported by the Ministry of Economic Affairs and falls under the Topsector Water & Maritime, contract number T-DEL/2021/024.

References

[1] A. G. Davenport, “The buffeting of structures by gusts,” in *Wind effects on Buildings and Structures*, T. M. National Physical Laboratory, Ed., vol. 1, Her Majesty’s stationery office, 1965.

[2] H. Natke, “Identification of the aerodynamic admittance function,” *IFAC Proceedings Volumes*, vol. 18, no. 5, pp. 657–662, 1985.

[3] C. P. W. Geurts, *Wind-induced pressure fluctuations on building facades*. Eindhoven: Technische Universiteit Eindhoven, 1997.

[4] Y. Zhou and A. Kareem, “Aerodynamic admittance function of tall buildings,” 2003.

[5] R. C. Aster, B. Borchers, and C. H. Thurber, *Parameter Estimation and Inverse Problems* -. Amsterdam: Elsevier, 2018, ISBN: 978-0-128-13423-8.

[6] S. L. Clainche and J. M. Vega, “Higher order dynamic mode decomposition,” *Journal on Applied Dynamical Systems*, vol. 16(2), pp. 882–925, 2017.

An optimised Numerical Method for the Third-Order Stochastic Dynamic Response computation of large MDOFs systems subjected to Non-Gaussian Turbulent Wind Loading

Michele Esposito Marzino[1]*, Vincent Denoël[2]

[1] *Structural and Stochastic Dynamics, University of Liège, Liège, Belgium*
[2] *Structural and Stochastic Dynamics, University of Liège, Liège, Belgium*
***Corresponding author**: michele.espositomarzino@uliege.be

Abstract
Stochastic dynamic analysis of structures to turbulent wind loading has been widely recognised since its conception back in 1961 for its effectiveness and computational power with respect to classical deterministic, time domain Monte Carlo simulations. In the last two decades, evidence along many studies have shown the importance to consider the non-Gaussian nature of the loading process. In such context, higher-order stochastic – dynamic – analysis (HOSA) is required. Thus, this work aims at providing an optimised numerical algorithm for the computation of the third-order skewness coefficients of the structural response of large Multi Degree-of-Freedom (MDOFs) systems, which overcomes the known burdens of the computation of higher-order spectra in a non-Gaussian context.

Keywords
buffeting, non Gaussian, bispectral

1. Introduction

Wind induced vibrations may play a crucial role for flexible structures, such as long-span bridges, tall buildings, large-span roofs [3]. These are large structures where often one dimension is some order of magnitude greater than others, flexible enough to exhibit important dynamic response to wind loading, for which the main assumption, made in common code standards, of response in its main mode of vibration may – and almost always does – not hold. In these cases, structural engineers opt for a measured and/or computed aerodynamic pressure field to perform the buffeting analysis. The subsequent structural analysis might be carried either in time or frequency domain, as well as in a nodal, modal or hybrid basis. For example, buffeting analysis in a Gaussian context – as quite always assumed in all studies carried in this context [8] – is typically handled by a spectral analysis following the Davenport Chain. In this analysis, the Power Spectral Density (PSD) of the structural response can be obtained through a sequential multiplication of the turbulence components PSDs', an aerodynamic and a mechanical admittance [3]. This approach has undoubted analytical advantages since, in case of linear mechanical structural behaviour, the structural response happens to be Gaussian too [6], so it can be fully characterised by the first two statistical moments only [8] – mean and variance.

However, even assuming a Gaussian process for the three random wind turbulent components in space $u(t)$, $v(t)$, $w(t)$, wind pressure is known to be a priori non-Gaussian, because of the nonlinear transformation of wind velocities to wind pressure, see e.g. [5]. Indeed, for common structures subjected to wind, due to the low turbulence intensity of common winds, the effects of the quadratic terms on most of the civil structures might be neglected [2]. In [9], it is shown how for increasing wind turbulence intensities, the actual Probability Density Function (PDF) of the wind pressure obtained from wind velocities, rapidly diverges from a Gaussian-like distribution if the quadratic term is considered. Also, [10] points out that even though the quadratic term of the wind turbulence does lead to actual small relative error in the estimation of the wind force, what is actually important is the frequency energy distribution of the non-linear process, which

might be close to the dynamics of the system. Hence, there might be cases in which neglecting the quadratic term can lead to significant overestimations or underestimations of the structural response. Indeed, both scenarios are not suitable, the former because of economic interests, the latter because of safety risks.

Therefore, if the statistical description of input and/or output in a given system differs from Gaussian, conventional methodologies as previously stated may no longer be valid in order to ensure safety and reliability of structures [11].

2. Context

In the context of non-linear buffeting analysis, where the wind loading follows a-priori a non-Gaussian probability distribution, the stochastic approach would require the evaluation of higher-order statistical moments – higher than the second – to properly characterise and quantify the diversion of the PDF of the structural response from a Gaussian-like distribution, when a closed form expression of such a PDF cannot be determined [1]. This requires the evaluation of higher-order spectra, which increases the complexity, in conceptual as well as practical terms. In the theory of probability, higher order statistical descriptors that quantify non-Gaussian variables are the skewness, 3$^{\text{rd}}$ order descriptor, which quantifies the asymmetry, and the kurtosis or excess, at 4$^{\text{th}}$ order, which quantify the flattening of the tails of the PDF distribution. As of today, even though the wind engineering community is starting to increasingly admit the non-Gaussianity of the wind loading, almost never it is actually taken into account for many reasons [7]. As stated above, 2$^{\text{nd}}$ order stochastic dynamic analysis has taken the place since the middle of 20$^{\text{th}}$ century. This means that the wind engineering community has now more than 50 years of expertise with such an approach alongside to classical, deterministic time domain resolution, with the use of well-known numerical algorithms developed to optimise these kinds of problems – parallel to the increase in the computational power provided by common PCs. Additionally, the concept of a power spectrum, even though much more abstract at a first sight with respect to a time series of the recorded wind pressure acting on a given pressure-tap from a wind tunnel test, was and is still concrete enough in a physical sense for civil engineers to be applied with relative ease.

Nonetheless, as to the non-Gaussian nature of the wind loading, there exist analytical solutions for the computation of power spectrum and bispectrum of aerodynamic wind forces as a combination of the PSDs of the wind turbulent components $u(t)$, $v(t)$, $w(t)$, by means of Volterra Series expansions and Fourier analysis, see e.g. [4]. These expressions are not much more complicated than the usual 2nd spectral analysis.

Focusing on the higher-order spectra, the bispectrum of the wind loading can be expressed as

$$\mathbf{B}_f = f(\mathbf{S}_u, \mathbf{S}_v, \mathbf{S}_w) \tag{1}$$

being $\mathbf{S}_u$, $\mathbf{S}_v$, $\mathbf{S}_w$ the PSDs of the three elemental wind turbulence components, assumed to be Gaussian random processes. Then, following the same concept as of for the second order, the spectra of the response – in nodal or modal basis – is the result of the multiplication of the loading spectra and a kernel:

$$\mathbf{B}_q(\omega_1, \omega_2) = \mathbf{K}_B(\omega_1, \omega_2)\, \mathbf{B}_{f^*}(\omega_1, \omega_2) \tag{2}$$

where

$$\mathbf{K}_B(\omega_1, \omega_2) = \mathbf{H}(\omega_1)\, \mathbf{H}(\omega_1)\, \mathbf{H}^*(\omega_1 + \omega_2) \tag{3}$$

where $\mathbf{H}(\omega)$ is the structure Frequency Response Function (FRF), the * operator indicates the complex conjugate.

If $x(t)$ is a zero-mean non-Gaussian random process, then the third statistical moment is given by

$$m_{3,x} = \iint_{-\infty}^{+\infty} \mathbf{B}_x(\omega_1, \omega_2)\, d\omega_1 d\omega_2 \tag{4}$$

Coupling bispectral analysis with the well-known 2$^{\text{nd}}$ order spectral analysis, the skewness coefficient is given by

$$\gamma_{3,x} = \frac{m_{3,x}}{m_{2,x}^{\frac{3}{2}}} \tag{5}$$

being $m_{2,x}$ the second order statistical moment, obtained from the PSD as

$$m_{2,x} = \int_{-\infty}^{+\infty} \mathbf{S}_x(\omega)\, d\omega \tag{6}$$

3. Preliminary results

As of today, no proof of application of bispectral analysis to real MDOFs structures is found. Indeed, some authors have applied it to very small structures (< 10 DOFs, [8]). The reasons are found in the very high computational costs required in:

- Projecting the `NDOFs` $\times$ `NDOFs` $\times$ `NDOFs` 3D matrix of wind forces $\mathbf{B}_f(\omega_1, \omega_2)$ in (1) in the modal

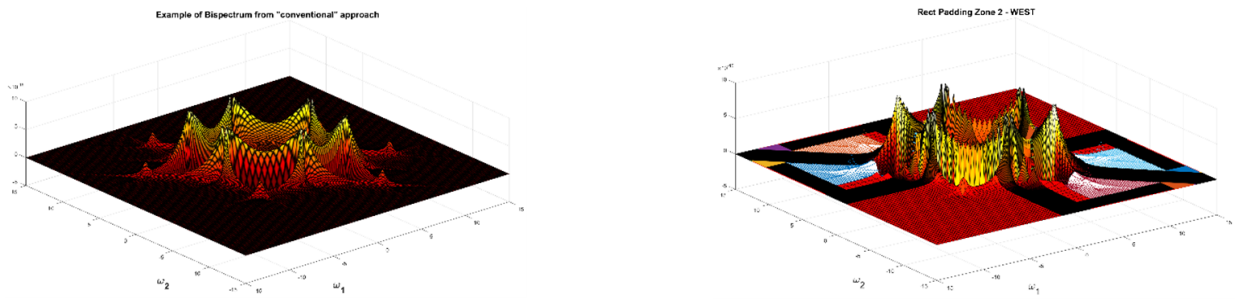

(a) (b)

Figure 1. (a) example of auto-bispectrum from classic approach. (b) illustration of the same spectrum, with the proposed method representation.

basis, for each pair of frequencies (ω_1, ω_2) of the discretised 2D frequency space

$$\mathbf{B}_{f^*_{mno}}(\omega_1, \omega_2) = \sum_{i=1}^{\texttt{NDOFs}} \sum_{j=1}^{\texttt{NDOFs}} \sum_{k=1}^{\texttt{NDOFs}} \phi_{im}\, \phi_{jn}\, \phi_{ko}\, \mathbf{B}_f(\omega_1, \omega_2) \tag{7}$$

This is the most expensive operation.

- Performing the double integration in (4) in the frequency space of $B_{q,mno}$ bispectrum of the structural modal responses for each combination of mode triplets (m,n,l), e.g. $\texttt{NMODES}^3$ a-priori double integrations.

To give an example, considering a relatively small structure with 10 degrees of freedom (NDOFs), 5 vibration modes, and a frequency space discretisation of 500×500, to recover the entire 3D matrix of $\mathbf{B}_q$ it is needed roughly

$$500 \cdot 500 \cdot 5 \cdot 5 \cdot 5 \cdot 10 \cdot 10 \cdot 10 = 3.125 \cdot 10^{10}$$

operations, without having considered the double integration in (4). With dimensions of usual real structures, it is instantly clear how this operation becomes the burden with current CPUs power in a feasible amount of time – say, less than a day. Indeed, together with CPU time, it should not be forgotten the amount of memory storage needed to store and process this much of information.

With this in mind, and with the goal of making bispectral analysis appealing for its application to relatively large structures of some hundreds of DOFs or more, an optimised numerical algorithm has been developed to tackle the most demanding aspects without sacrificing too much precision with respect to the canonical application of eqs. (1) and (2). Indeed, a very important aspect to not forget is the even what is addressed as the canonical approach, is an approximation, since a closed-form solution to such a problem does not – yet – exist. The proposed method is based on some basic concepts, which have been fitted ad-hoc to the considered problem, still leaving space for some sort of generalisation:

- Subdivision of the frequency space into an ensemble of points grouped into basic, independent geometrical shapes (rectangles, triangles), at which, in a first stage, the loading information (bispectrum, $\mathbf{B}_f(\omega_1, \omega_2)$) is computed.
- Data interpolation for an efficient and smart computation of $\mathbf{B}_x(\omega_1, \omega_2)$, bispectrum of the structural response.

4. Conclusions

First developments have shown an important step toward making bispectral analysis more appealing to a wider range of day-to-day applications. Though its application to very small structures has shown no significant improvement in CPU time – mostly because of the non-negligible overhead in the patching of the frequency space – its effectiveness has proven as soon as the dimensions of the problem increase. Figure 1 shows an example of an auto-bispectrum – i.e. the three indexes (m,n,o) are the same, $m = n = o$ – from the two main imlpementations, classical and the proposed methodology. Figure 2 shows an example of CPU time evolution between different approaches and imlementation of BSA – Bispectral Stochastic Analysis – which proves the fact that the method has its interest as soon as dimensions become important.

5. Aknowledgements

Part of this research project has been supported thanks to a research project funded by the Walloon Region (Convention Nb. 8096, FINELG2020).

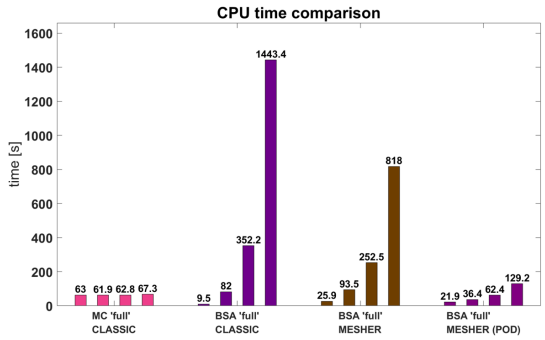

Figure 2. Example of CPU timings evolution between different BSA methods with increasing number of loaded `DOFs` for a given structure.

References

[1] S. Benfratello, S. Caddemi, and G. Muscolino. "Gaussian and Non-Gaussian stochastic sensitivity analysis of discrete structural system". In: *Journal of Computers and Structures* 78 (2000), pp. 425–434.

[2] S. Benfratello, G. Falsone, and G. Muscolino. "Influence of the quadratic term in the along-wind stochastic response of SDOF structures". In: *Journal of Engineering Structures* 18 (1996), pp. 685–695.

[3] W. Cui, L. Zhao, and Y. Ge. "Non-Gaussian turbulence induced buffeting responses of long-span bridges based on state augmentation method". In: *Journal of Engineering Structures* 254 (2022), pp. 432–439.

[4] V. Denoël. "Application des méthodes d'analyse stochastique à l'étude des effets du vent sur les structures du génie civil". PhD thesis. University of Liège, 2005.

[5] V. Denoël. "Polynomial approximation of aerodynamic coefficients based on the statistical description of the wind incidence". In: *Journal of Probabilistic Engineering Mechanics* 24 (2009), pp. 179–189.

[6] M. Gioffrè, V. Gusella, and M. Grigoriu. "Non-Gaussian Wind Pressure on Prismatic Buildings". In: *Journal of Structural Engineering* 127 (2001), pp. 981–989.

[7] K. R. Gurley, M. A. Tognarelli, and A. Kareem. "Analysis and simulation tools for wind engineering". In: *Journal of Probabilistic Engineering* 12(1) (1997), pp. 9–31.

[8] V. Gusella and A. L. Materazzi. "Non-Gaussian Response of MDOF Wind-Exposed Structures: Analysis by Bicorrelation Function and Bispectrum". In: *Journal of Meccanica* 33 (1998), pp. 299–307.

[9] J. D. Holmes. "Non-Gaussian Characteristics Of Wind Pressure Fluctuations". In: *Journal of Wind Engineering and Industrial Aerodynamics* 7 (1987), pp. 103–108.

[10] A. Kareem. "Nonlinear wind velocity term and response of compliant offshore structures". In: *Journal of Engineering Mechanics* 110 (1984), pp. 1573–1578.

[11] D.-K. Kwon and A. Kareem. "Gust-Front Factor: New Framework for Wind Load Effects on Structures". In: *Journal of Structural Engineering* 135 (2009), pp. 717–732.

Third-order spectral analysis of an oscillator subjected to wind loads with complex-valued bispectrum

Margaux Geuzaine[1]*, Michele Esposito Marzino[1], Vincent Denoël[1]

[1] *Structural & Stochastic Dynamics, Urban & Environmental Engineering, University of Liège, Belgium*
[2] *Department of Aerodynamics, University of Something, Beijing, China*
***Corresponding author**: mgeuzaine@uliege.be

Abstract
The third-order spectral analysis of an oscillator subjected to time-irreversible wind loads is conducted in this paper. It is proposed to evaluate the statistics of the oscillator's response otherwise than through the numerical integration of the corresponding spectra, in order to avoid the computational burden associated with this operation. To this aim, the Multiple Timescale Spectral Analysis is used. This framework generalizes the Background/Resonant decomposition and offers a rapid yet accurate way to estimate the statistics of the structural responses at any order. In particular, it recently allowed to derive simple approximate expressions for the third central moments of the structural responses obtained under such a specific loading whose bispectrum is actually complex-valued. These formulas are presented in this paper and are eventually shown to provide precise results for the computation of statistics, 100 times faster than before.

Keywords
Bispectrum, Skewness, Background, Bi-Resonant, Time-Irreversible, Non-Gaussian

1. Introduction

In a spectral context, the second and third cumulants of real-valued processes are typically obtained by integrating the real parts of their power spectral density and their bispectrum over a one- and a two-dimensional frequency space, respectively. When dealing with the response of a slightly damped oscillator whose natural frequency is much higher than the characteristic frequency of the loading as it is typical in wind engineering, these spectra are however expected to feature sharp peaks and their numerical integration requires using a lot of points to provide sufficiently accurate results.

From a perturbation perspective, the distinctness of the peaks in the functions to integrate can fortunately be turned into an advantage [10]. The contributions of such separated peaks to the integral can be considered sequentially and be expressed by easily interpretable semi-analytical formulas. Regarding the variance, it yielded the famous background/resonant decomposition, which is widely used by the wind engineering community [2].

Then, it allowed to formalize the general framework of the Multiple Timescale Spectral Analysis, which helps to find similar expressions for higher order or crossed statistics [4]. They are eventually computed much faster than before thanks to the resulting reduction in the dimension of the integrals.

In previous works [5, 3], the third cumulant of a linear oscillator's response to non-Gaussian wind forces has already been decomposed into two parts. To do so, the imaginary part was completely discarded in the bispectrum of loading. This assumption is licit provided that it is a time-reversible process, e.g. a memoryless transformation of a Gaussian input such as the wind velocity. In this event, the imaginary part in the bispectrum of loading is in fact exactly equal to zero everywhere [12].

But in a more general context, it can be significant, although no wind load model is currently able to produce a complex-valued bispectrum. Experimental evidences show that the imaginary part might even be of the same order of magnitude as the real part [6], see the example in Figure 2 which is based on the data collected by [1].

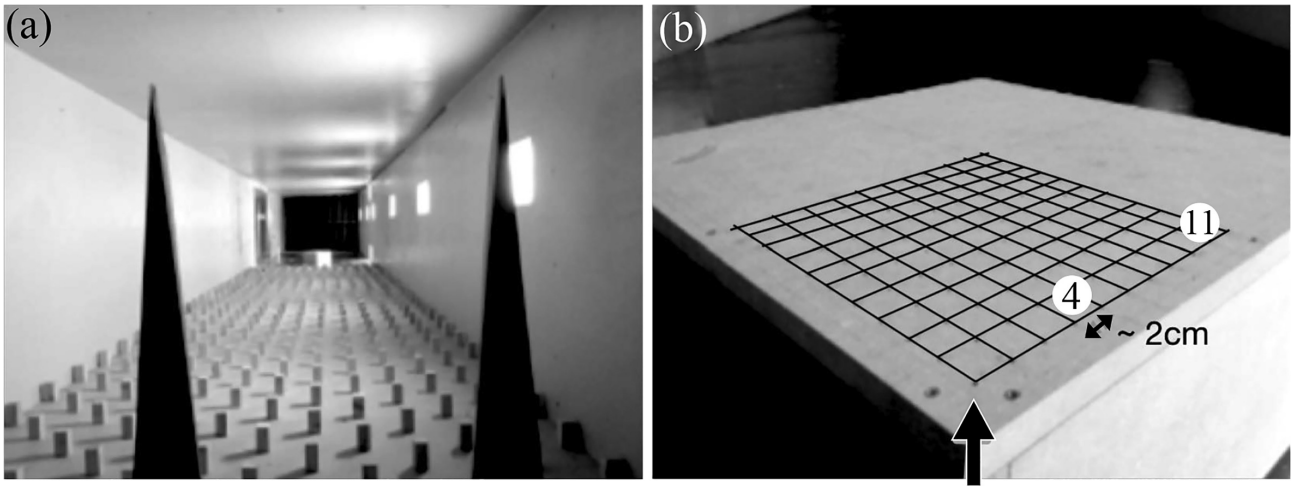

Figure 1. **(a)** Experimental setup in the wind tunnel. **(b)** Location of pressure taps and direction of the wind. [1]

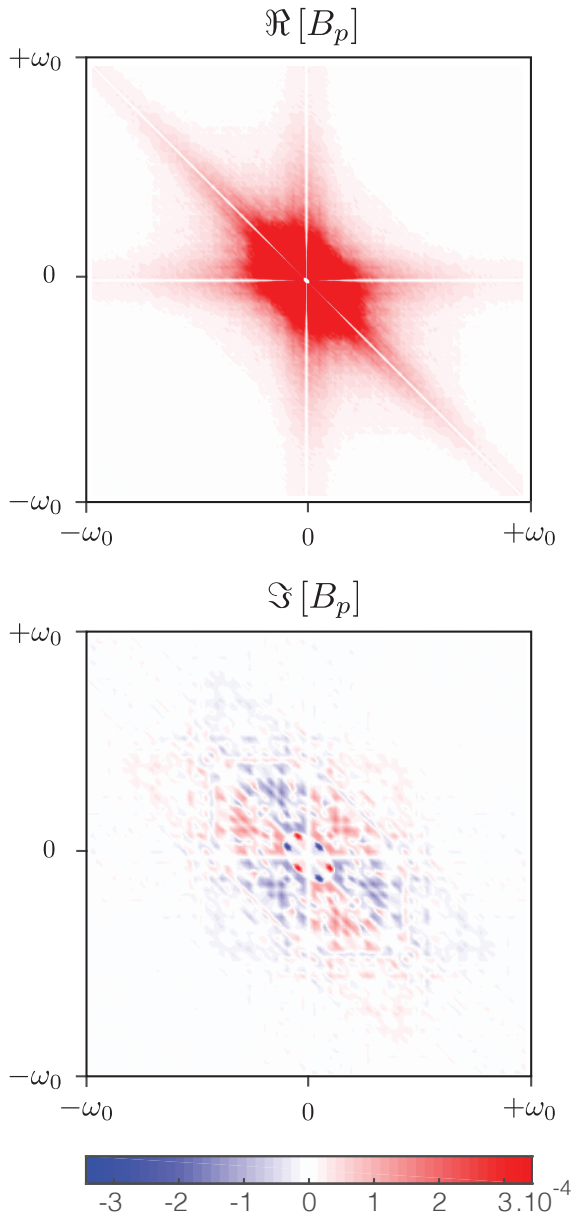

Figure 2. Bispectrum of the wind pressures recorded on the experimental setup on tap n°4.

2. Motivation

In the context described above, the bispectrum of the oscillator's response is theoretically given by

$$B_q(\omega_1,\omega_2) = B_p(\omega_1,\omega_2)K_3(\omega_1,\omega_2) \tag{1}$$

where $B_p(\omega_1,\omega_2)$ is the bispectrum of the loading and $K_3(\omega_1,\omega_2)$ is the structural kernel of the oscillator at third order [3]. It is more specifically given by

$$K_3(\omega_1,\omega_2) = H_x(\omega_1)H_x(\omega_2)H_x^*(\omega_1+\omega_2) \tag{2}$$

where the star superscript denotes the conjugate operation, and depends on the frequency response function

$$H_x(\omega) = (k_s - m_s\omega^2 + 2\imath\omega\xi\sqrt{k_s m_s})^{-1} \tag{3}$$

of the oscillator with k_s being its stiffness, m_s being its mass, ξ being its damping ratio, and hence $\omega_0 = \sqrt{k_s/m_s}$ being its natural frequency.

The third cumulant of the oscillator's response can then be obtained by integrating the corresponding bispectrum as follows

$$\kappa_{3,q} = \iint \Re[B_q(\omega_1,\omega_2)]\mathrm{d}\omega_1\mathrm{d}\omega_2 \tag{4}$$

where

$$\begin{aligned}\Re[B_q(\omega_1,\omega_2)] = \Re[B_p(\omega_1,\omega_2)]\Re[K_3(\omega_1,\omega_2)] \\ - \Im[B_p(\omega_1,\omega_2)]\Im[K_3(\omega_1,\omega_2)]\end{aligned} \tag{5}$$

while the imaginary part of $B_q(\omega_1,\omega_2)$ does not contribute for symmetry reasons. This is in line with the fact that the cumulants of any real-valued process are real-valued as well.

On the one hand, if the imaginary part of the loading bispectrum is negligible, the product of the imaginary parts drops in Eq.(5) and the same conditions as in

[Denoël 2011] are met. Using the Multiple Timescale Spectral Analysis in this particular case then, as in [Denoël 2015], shows that the third cumulant can be decomposed into a sum of two major contributions. The first one

$$\kappa_{3,b} = \frac{\kappa_{3,p}}{k_s^3} \tag{6}$$

is referred to as (tri-)background and the second component

$$\kappa_{3,r} = 6\pi \frac{\omega_0^3}{k_s^3} \xi \int \frac{\Re\left[B_p\left(\omega_0, \omega_2\right)\right]}{\left(2\xi\omega_0\right)^2 + \omega_2^2} \, \mathrm{d}\omega_2 \tag{7}$$

is termed background-biresonant. These names indicate the origin of the peaks from which these contributions stem. In particular, the background component is due to the peak of the loading bispectrum which is located in the low frequencies. Meanwhile, the biresonance is associated with the crossing of two lines of poles in the frequency response functions which constitute the structural kernel.

On the other hand, if the imaginary part of the loading bispectrum is significant, an additional background-biresonant contribution has to be considered. It has more recently been expressed as

$$\kappa_{3,i} = 3\pi \frac{\omega_0^2}{k_s^3} \int \frac{\Im\left[B_p\left(\omega_0, \omega_2\right)\right]}{\left(2\xi\omega_0\right)^2 + \omega_2^2} \omega_2 \mathrm{d}\omega_2 \tag{8}$$

by using the Multiple Timescale Spectral Analysis. Details about the establishment of this formula can be found in [7].

However, until now, it was difficult to verify that the latter formula was correct and necessary, since wind models currently generate real-valued bispectra only, while experimental studies show that it can indeed be complex-valued. In this paper, these two questions are therefore addressed by means of an example for which it has been decided to estimate the bispectrum of loading through a parametric approach based on an auto-regressive loading model [11]. It is thus expressed as follows

$$B_p(\omega_1, \omega_2) = H_p(\omega_1) H_p(\omega_2) H_p^*(\omega_1 + \omega_2) \tag{9}$$

with

$$H_p(\omega) = \frac{1}{1 + \alpha i \omega} \tag{10}$$

where $\alpha = \omega_p / \omega_0$ stands for the frequency ratio between the characteristic frequencies of the wind load and the oscillator.

3. Parametric Analysis

Globally, the results presented in Figure 3-(h) and Figure 3-(i) can be explained quite easily thanks to the simple expressions that have been obtained for the main components of the third central moment of the response.

First, the approximations provided by their sums are verified as their ratio with the reference values are close to one and are getting even closer when the frequency ratio and the damping ratio decrease. This is indeed to be expected given that the multiple timescale spectral analysis is based on perturbation methods and its accuracy is consequently conditioned upon the smallness of these two parameters.

Second, the background to bi-resonant ratio decreases with the damping ratio. By contrast, the bi-resonant component increases with the frequency ratio. Small damping ratios and large frequency ratios result in a relatively more resonant structural response, which is less skewed and thus more Gaussian, as shown in Figure 3-(i). This corroborates the central limit theorem.

At last, the bi-resonant component related to the imaginary part of the loading bispectrum is clearly not negligible in the example at stake.

4. Conclusions

Thanks to the meaningful analytical expressions provided by the Multiple Timescale Spectral Analysis for the third central moments of the oscillator's response, it appears that a significant contribution can sometimes be attributed to the existence of an imaginary part in the bispectrum of loading.

This raises a question about the validity of traditional wind load models in some circumstances, given that they are only able to produce real-valued bispectra of forces. New wind load models, which create time-irreversible processes with complex-valued bispectra, should therefore be proposed in the future to solve this problem.

But overall, the Multiple Timescale Spectral Analysis is already able to deal with the response of an oscillator subjected to such a loading process. The expressions detailed in Section 2 help to understand how the response is influenced by the loading and by the structural parameters, respectively. They thus allow to determine how the structure can be modified to exhibit a safer dynamical behavior, based on simple and sound mathematics.

Hinging on the perturbation theory, the discrepancy is also known to remain limited provided that the damping ratio and the frequency ratio are sufficiently

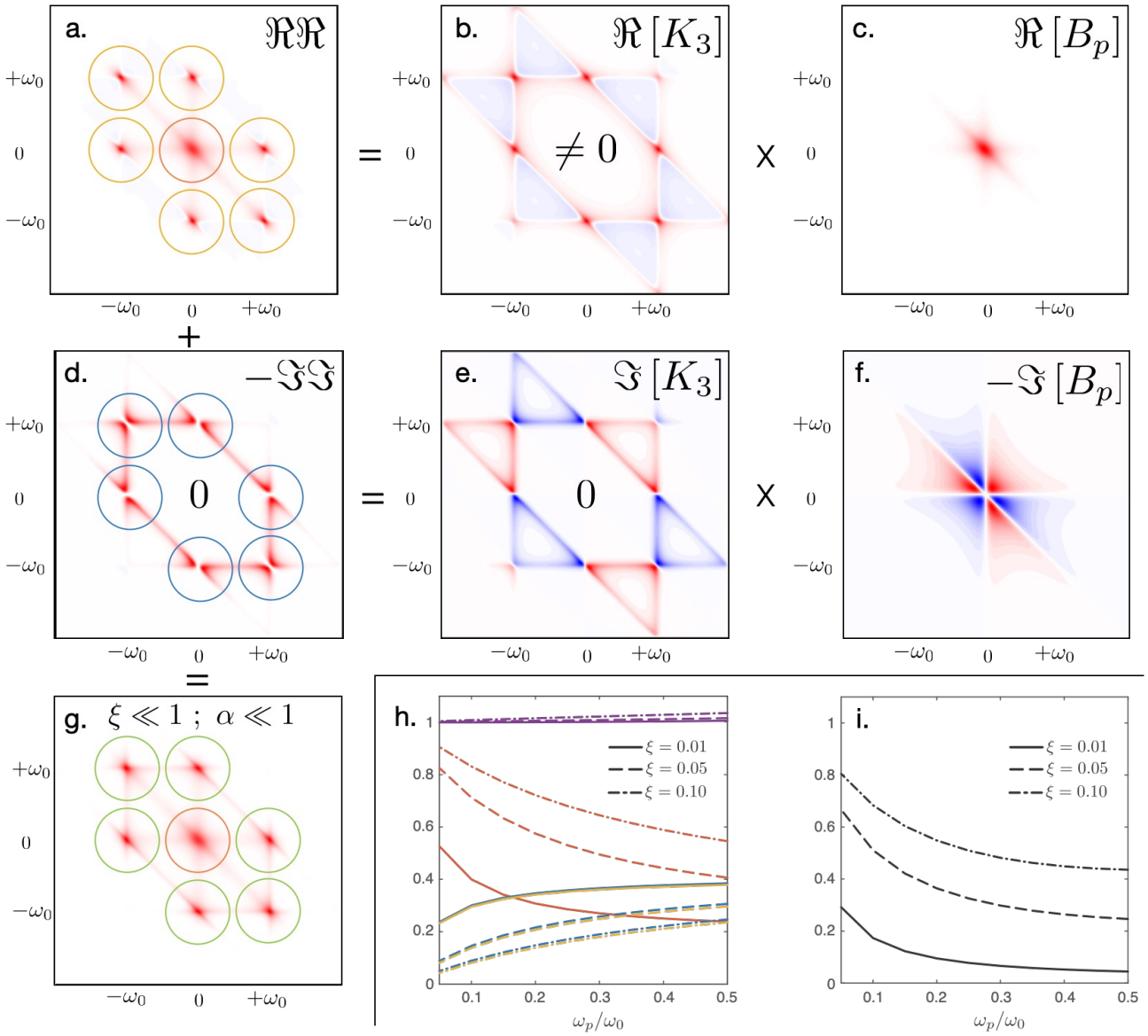

Figure 3. (a) Product of (b) and (c) with (b) the real part of the structural kernel and (c) the real part of the loading bispectrum. (d) Minus the product of (e) and (f) with (e) the imaginary part of the structural kernel and (f) the imaginary part of the loading bispectrum. (g) Sum of (a) and (d), which gives the real part of the response bispectrum. (h) In purple, the ratio between the third central moments of the response obtained through the proposed decomposition and through the numerical integration of the bispectrum, then in orange, yellow and blue, the distribution of the estimated results between the background and the bi-resonant components associated to either the real part, either the imaginary part of the loading bispectrum, respectively. (i) Dynamic amplification of the skewness of the response with respect to the skewness of the loading.

smaller than unity. Last but not least, the computational time is divided by about one hundred at least when using the expressions derived in this paper for the third central moments of the responses. This is explained by the fact that integrating their bispectrum over a two-dimensional frequency space is avoided.

The Multiple Timescale Spectral Analysis has thus proved its worth and is currently being developed to provide such expressions for the statistics of structures with many degrees-of-freedom, subjected to self-excited forces [9], or wave forces which trigger the inertial regime as well [8], on top of the background and the resonant ones.

5. Acknowledgements

The first author gratefully thanks the F.R.S.-FNRS, the Belgian Fund for Scientific Research, for the financial support they provided her through a FRIA PhD Fellowship. The second author was also financially supported by the FineLg2020 project of the Walloon Region.

References

[1] N. Blaise, T. Andrianne, and V. Denoël. "Assessment of extreme value overestimations with equivalent static wind loads". In: *Journal of Wind Engineering and Industrial Aerodynamics* 168 (2017), pp. 123–133.

[2] A. G. Davenport. "The spectrum of horizontal gustiness near the ground in high winds". In: *Quarterly Journal of the Royal Meteorological Society* 87.372 (1961), pp. 194–211.

[3] V. Denoël. "On the background and biresonant components of the random response of single degree-of-freedom systems under non-Gaussian random loading". In: *Engineering Structures* 33.8 (2011), pp. 2271–2283.

[4] V. Denoël. "Multiple timescale spectral analysis". In: *Probabilistic Engineering Mechanics* 39 (2015), pp. 69–86.

[5] V. Denoël and L. Carassale. "Response of an oscillator to a random quadratic velocity-feedback loading". In: *Journal of Wind Engineering and Industrial Aerodynamics* 147 (2015), pp. 330–344.

[6] M. Esposito Marzino et al. "Bispectrum and Bicorrelation: a higher order stochastic approach to non-Gaussian Dynamic Wind Loading". In: (2019).

[7] M. Geuzaine. "Multiple Timescale Spectral Analysis of Wave-Loaded Floating Structures". In: (2022).

[8] M. Geuzaine and V. Denoël. "Efficient estimation of the skewness of the response of a wave-excited oscillator". In: *Proceedings of the XI International Conference on Structural Dynamics, EURODYN 2020* (2020), pp. 3467–3480.

[9] J. Heremans, A. Mayou, and V. Denoël. "Perspectives on the acceleration of the numerical assessment of flutter and buffeting response of bridge decks". In: *COMPDYN Proceedings* 2021-June.October (2021).

[10] E. Hinch. *Perturbation Methods*. Ed. by Cambridge University Press. Cambridge: Cambridge University Press, 1995.

[11] M. R. Raghuveer and C. L. Nikias. "Bispectrum Estimation: A Parametric Approach". In: *IEEE Transactions on Acoustics, Speech, and Signal Processing* 33.5 (1985), pp. 1213–1230.

[12] M. L. Williams. "The use of the bispectrum and other higher order statistics in the analysis of one dimensional signals." In: July (1992), pp. 51–73.

Full-scale wind pressure measurements on the Space Needle

John Hochschild[1]*, Catherine Gorlé[1]

[1] *Civil and Environmental Engineering, Stanford University, Stanford, California*
***Corresponding author**: jhochsch@stanford.edu

Abstract
To better understand and evaluate established methods modeling of peak pressures on high-rise building cladding panels, absolute pressure measurements were taken at full-scale on the Space Needle. A sensor was selected that can make meaningful C_p measurements at windspeeds as low as 10 m/s and a custom sensing mote was designed for long-term deployment on high-rises. A network of motes was deployed on the Space Needle, but due to connectivity issues, pressure statistics were gathered at only 5 locations. These measurements alone will be useful for comparison with wind tunnel and computational results, but more measurements will be acquired by switching to Wifi-enabled motes and re-deploying 24 motes on the Space Needle roof.

Keywords
full-scale measurements, peak pressures

1. Introduction

The cost of damage to buildings and infrastructure due to global extreme weather is estimated to be $150 billion annually [1], with a significant portion due to wind events [10]. Observations of damage and surveys of insurance claims show that the majority of damage from extreme wind events is to the building envelope rather than its structure [8, 11]. Improving our understanding and modeling of wind loads on building envelope components will enable resilient design to alleviate damage and the resulting social upheaval.

Currently, wind loads on building envelopes are estimated either using building codes and standards, which are based on empirical information from wind tunnel pressure measurements on canonical building shapes, or using dedicated wind tunnel measurements for the specific building under consideration. There are two important limitations to this approach. First, there is uncertainty in the estimated peak wind loads on envelope elements because of the limited spatial resolution of the pressure measurements in wind tunnel experiments. To accurately calculate the overall load on a cladding panel, multiple pressure tap measurements should be obtained on that single panel; however, in current practice it is often not even feasible to have even a single pressure tap on each high-rise building panel. As a result, additional post-processing is needed to approximate the area-averaged peak pressure load on a panel. This post-processing usually takes the form of applying a time-filter to represent the effect of limited spatial correlation and the time-scale used for the filter operation is an important source of uncertainty [5].

Second, it is assumed that the peak pressure loads generated on a scaled wind tunnel model are representative of those experienced by a full-scale building. Previous studies have compared wind loads measured at full- and model-scale on low-rise structures and consistently found peak pressures to be underestimated at the wind tunnel scale [9] [7] [6] - an alarming finding. On larger high-rise buildings there is a lack of data comparing full- and model-scale loads. One experiment in the 1970s involved taking full scale measurements at 32 locations on a 57-floor Toronto skyscraper [4]. Although this data shows agreement between full- and model-scale measurements for both mean and peak pressures, it is limited because the use of differential sensors meant changes in the building's internal pressure made measurements more uncertain.

To improve our understanding and prediction of peak pressure loads on envelope elements, we seek to directly measure full-scale wind pressures acting on high-rise buildings. Unlike in [4], we will use absolute pressure sensors to preclude uncertainties associated with the dynamic internal building pressure. These measurements will be useful for evaluating the use

and quantifying the accuracy of wind tunnel testing and computational fluid dynamics (CFD) models for predicting wind loads on high-rises.

2. Methods

2.1 Sensing Mote Design

Environmental sensing networks are traditionally made up of individual 'motes', which comprise a datalogger, sensor, and power electronics. We designed a custom mote for the purposes of this investigation. The mote was designed to be low-profile and unobtrusive so as not to significantly influence the flow, as well as wireless and solar-powered to be able to gather data over many months. The resulting Arduino-based design is open-source and can be used with almost any I2C or SPI sensor, making it suitable for almost any environmental sensing application.

The mote housing was designed to accommodate a solar panel, three sensors, and other electronics. It is 3D printed in white to minimize solar heating. The housing schematic is shown in Figure 1 and a photo of a mounted mote is shown in Figure 2.

The absolute pressure sensor used is the Bosch Sensortec BMP388 [2]. This sensor was selected after testing four candidate absolute sensors in a wind tunnel and finding the BMP388's signal-to-noise ratio to be sufficiently high to make meaningful C_p measurements when $U > 10$ m/s. Because this sensor allows us to measure C_p at relatively low windspeeds, we can gather more data and are less geographically limited. Each mote has three BMP388 sensors with ports on different faces so that we can quantify the effect of orientation and housing geometry.

At the core of each mote is a Wifi- or cellular-connected Arduino board, specifically either the MKR WiFi 1010 or MKR 1500 NB. Most of the time the board sleeps to conserve battery power, but wakes to check the windspeed every 20 minutes. If the windspeed exceeds some defined threshold, the motes will wake and start acquiring data until commanded to stop. The solar panel provides sufficient power for a few hours of acquisition per day, depending on climate and orientation.

2.2 Field Deployment

The Space Needle in Seattle, WA was chosen because it is a tall building with only low-rise buildings upstream, minimizing difficulties modeling interference effects from surrounding buildings. In addition, circular geometries tend to be particularly susceptible to scaling, so the building geometry makes for an interesting comparison with scaled experiments and simulations.

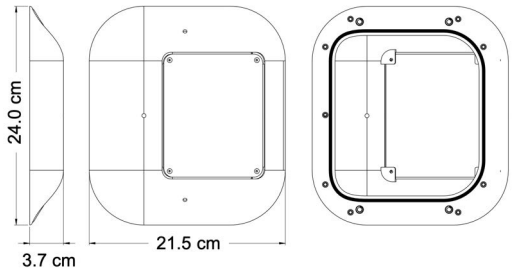

Figure 1. Three-view schematic of mote housing.

Figure 2. Mote mounted on a wall with magnets.

In February 2022, motes were mounted on the upper (flat) and main (sloped) roofs of the Space Needle. The sensors were installed using 3M VHB tape, which stayed adhered very well over many months despite the harsh conditions at the top of the building. One sensor installed on the building is shown in Figure 3.

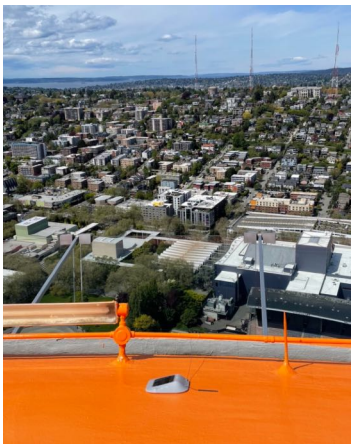

Figure 3. One mote mounted on the Space Needle's sloped roof.

Connectivity issues impeded the initial deployment: most sensors were not connecting frequently enough to gather usable data. We discovered the cause to be that the Arduino MKR 1500 NB board will not connect to T-Mobile's Band 2 LTE network, even though it is rated for Band 2. In other locations, the board connects to T-Mobile's Band 12, but we found there to be poor reception in this band at the top of

the Space Needle. The situation was ameliorated in May 2022 by installing a cellular booster at the top of the building to extend Band 12. Although doing so improved connectivity, some sensors still struggled to connect: of the 14 sensors installed, only 5 gathered useful amounts of data. The locations of these 5 sensors are shown in Figure 4.

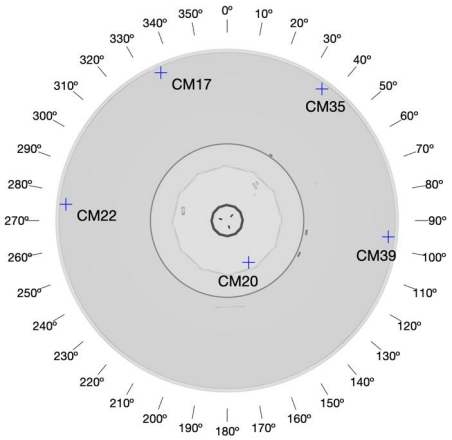

Figure 4. Location of motes on Space Needle roof, top view.

Windspeed measurements were gathered by a Gill WindSonic anemometer installed at the top of the building, as shown in Figure 5. Reference sensors were placed inside the building at the top, and outside of the building at the base. The reference sensors also struggled with connectivity issues.

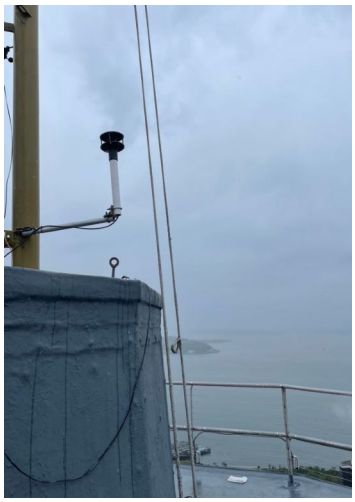

Figure 5. Anemometer mounted at the top of the Space Needle.

Lacking a reliable barometric reference measurement P_{ref}, we instead calculate and present ΔC_p statistics instead of the usual C_p statistics. ΔC_p is given by Eq. 1.

$$\Delta C_p = \frac{P(t) - \overline{P}}{\frac{1}{2}\rho U^2} \tag{1}$$

where $\overline{P}$ is the 10 minute moving mean of the fluctuating pressure $P(t)$, ρ is the density, and U is the windspeed at building height. Although calculating statistics in this way precludes measuring $C_{p,mean}$, it still yields the turbulent statistics, $\Delta C_{p,min}$ and $\Delta C_{p,rms}$, which are expected to be more sensitive to the incoming wind characteristics, geometrical scaling, and numerical model choices, and are hence the more important quantities to measure at full-scale.

3. Results

For each mote, pressure time series were divided into 15-minute intervals and statistics were calculated for each interval. In the following plots, datapoints with high variability in wind direction $\Delta\theta > 2^\circ$ are not plotted. Figure 6 plots $\Delta C_{p,min}$ and $\Delta C_{p,rms}$ as a function of wind direction, θ, for two of the five motes shown in Figure 4. Minimum values were calculated using the Cook and Mayne method [3]. The colors correspond to different acquisitions. Some acquisitions are missing for certain motes because the mote was not connected at that time due to low battery or connectivity issues. In the CM35 data, the different acquisition days collapse and a clear trend is seen with wind direction: $\Delta C_{p,min}$ is more negative and $\Delta C_{p,rms}$ is higher for more southerly wind directions. The magnitude of $\Delta C_{p,min}$ also correlates with $\Delta C_{p,rms}$, as expected. In the CM17 data however, we see consistently more negative $\Delta C_{p,min}$ values on two of the acquisition days (28 & 29 Jun).

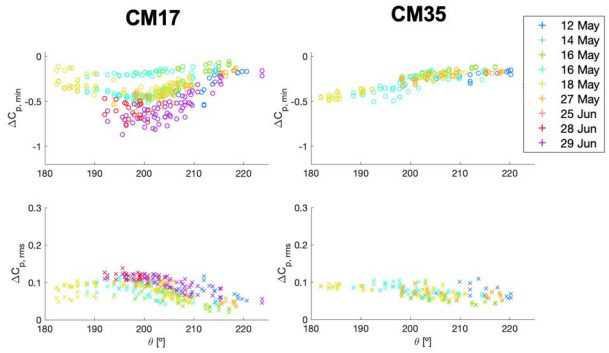

Figure 6. ΔC_p statistics as a function of wind direction for two of the motes, colored by acquisition period.

To further investigate these disparate trends, Figures 7 and 8 present the data recolored to correspond to which sensor on the mote measured each point, and the turbulence intensity as measured by the anemometer, respectively. Recalling that each mote has three sensors installed on different faces, we can investigate the variability of measurements by comparing the results

of sensors on a single mote, which is shown in Figure 7. Note that for CM35, rain ingress made one of the sensors inoperative.

From Figure 7, we can see that the larger variability is limited to the red and green sensors. This can possibly be explained by the fact that these sensors were on the mote housing's leeward side while the blue sensor was positioned on the windward side, and we would expect greater turbulence on the leeward side. A similar result was found for another mote, whose results are not shown here. These results suggest that the orientation of the housing does in fact effect the measured pressures.

Figure 8 shows that measurements during the highest turbulence intensity periods tend to give greater magnitude $\Delta C_{p,min}$ and $\Delta C_{p,rms}$ values, but it is not a perfect trend.

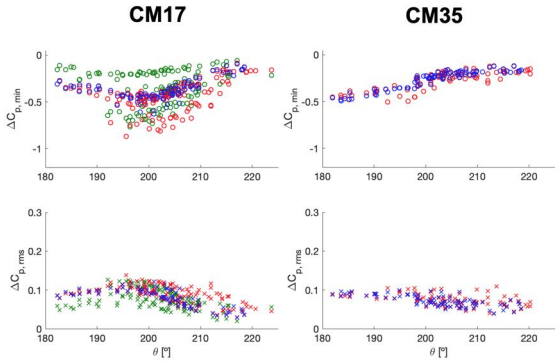

Figure 7. ΔC_p statistics as a function of wind direction for two of the motes, colored by sensor.

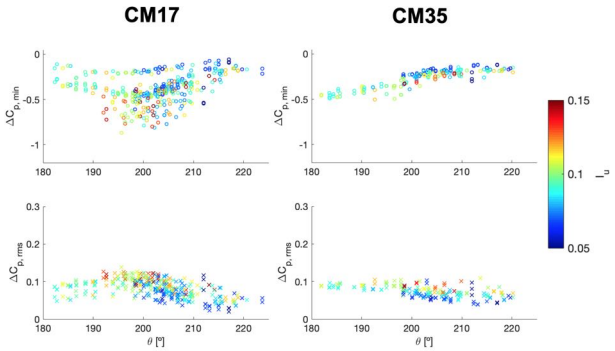

Figure 8. ΔC_p statistics as a function of wind direction for two of the motes, colored by turbulence intensity.

4. Conclusions

In an effort to gather full-scale absolute pressure measurements on a high-rise building, pressure sensing motes were placed on the roof of the Space Needle. Persistent connectivity issues prevented gathering reference pressure data and ΔC_p measurements at as many points as desired. Nevertheless, a large amount of data was gathered at five locations. Analysis of this data shows a potential influence of the mote housing. Therefore in future analysis, we will compare results from the three sensors on each mote, and for those that disagree we will take only the sensor measuring pressure on the mote's top surface, since this is parallel to the building surface. The data also showed the effect of turbulence intensity, thereby highlighting the importance of making comparisons with matched turbulence intensities.

Because of the cellular connection difficulties, the mote microcontrollers have been swapped out with Wifi-connected ones and a Wifi network has been installed at the top of the building. 24 Wifi-enabled motes and Wifi-enabled reference sensors will be installed on the Space Needle in November 2022 to gather data at more locations atop the building.

References

[1] S. Bienert. "Extreme weather events and property values". In: *Urban Land Institute* (2014).

[2] *BMP388: Digital pressure sensor*. BST-BMP388-DS001-01. Rev. 1.1. Bosch Sensortec. Mar. 2018.

[3] N. Cook and J. Mayne. "A refined working approach to the assessment of wind loads for equivalent static design". In: *Journal of Wind Engineering and Industrial Aerodynamics* 6.1-2 (1980), pp. 125–137.

[4] W. A. Dalgliesh, J. Templin, and K. R. Cooper. "Comparisons of wind tunnel and full-scale building surface pressures with emphasis on peaks". In: *Wind Engineering*. Elsevier, 1980, pp. 553–565.

[5] J. D. Holmes. "Equivalent time averaging in wind engineering". In: *Journal of Wind Engineering and Industrial Aerodynamics* 72 (1997), pp. 411–419.

[6] M. J. Morrison, T. M. Brown, and Z. Liu. "Comparison of field and full-scale laboratory peak pressures at the IBHS Research Center". In: *Advances in Hurricane Engineering: Learning from Our Past*. 2013, pp. 1109–1124.

[7] G. Richardson et al. "The Silsoe Structures Building: Comparisons of pressures measured at full scale and in two wind tunnels". In: *Journal of Wind Engineering and Industrial Aerodynamics* 72 (1997), pp. 187–197.

[8] P. Sparks, S. Schiff, and T. Reinhold. “Wind damage to envelopes of houses and consequent insurance losses”. In: *Journal of wind engineering and industrial aerodynamics* 53.1-2 (1994), pp. 145–155.

[9] H. Tieleman, D. Surry, and K. Mehta. “Full/model-scale comparison of surface pressures on the Texas Tech experimental building”. In: *Journal of Wind Engineering and Industrial Aerodynamics* 61.1 (1996), pp. 1–23.

[10] G. R. Walker. “Wind Disasters and the Insurance Industry”. In: *Proceedings of the Eleventh International Conference on Wind Engineering*. 2003, pp. 2293–2300.

[11] T. Williams and A. Kareem. “Performance of building cladding in urban environments under extreme winds”. In: *Proceedings of the 11th international conference on wind engineering, Lubbock*. Vol. 7. 2003.